

CO $J = 2-1$ MAPS OF BIPOLAR OUTFLOWS IN MASSIVE STAR-FORMING REGIONS

Y. WU,¹ Q. ZHANG,² H. CHEN,³ C. YANG,⁴ Y. WEI,¹ AND P. T. P. HO²

Received 2003 December 23; accepted 2004 September 28

ABSTRACT

Using the eight-beam array receiver of the NRAO 12 m telescope, we mapped the CO $J = 2-1$ emission toward 11 high-mass star-forming regions. In the sample, four are previously detected outflows in the CO $J = 1-0$ line, and seven are outflow candidates. A total of six bipolar outflows were identified in the CO $J = 2-1$ line. For the remaining five sources, including one previously detected bipolar outflow, the CO $J = 2-1$ emission shows multiple velocity components. Therefore, high-velocity line wings or bipolar structure cannot be identified. The CO $J = 2-1$ spectra of the four of the nonbipolar outflow sources exhibit broad-line emission due to the blending of weak velocity components. The complex CO spectra underscore the importance of large-scale mapping in identifying outflows. Compared with the outflows detected with the CO $J = 1-0$ line, the CO $J = 2-1$ outflows often have broader line wings and smaller spatial extents, indicating that the high-velocity gas measured with the CO $J = 2-1$ line arises from warm regions closer to the central source. The masses in the outflows range from a few to $60 M_{\odot}$. The linear momenta in the outflows are as large as a few hundred $M_{\odot} \text{ km s}^{-1}$. Both parameters are much larger than the typical values in low-mass outflows. The average dynamic timescale of the outflows is 2×10^4 yr. The driving sources of the bipolar outflows are also identified. All bipolar outflows detected have a near-infrared source, except for IRAS 23385+6053, and all are associated with centimeter or millimeter continuum emission, except for IRAS 22506+5549. We investigated the correlation between the outflow parameters and the properties of the driving source. The outflow luminosity and mechanical force correlate with the bolometric luminosity of the star. However, the mechanical force required to drive a CO outflow is more than an order of magnitude higher than the radiation pressure from the star. We reexamined the relation between the mass entrainment rate of the outflows and the bolometric luminosity of the central source with an up-to-date sample. Results show that the mass outflow rate increases with increasing bolometric luminosity, suggesting that the mass outflow rate is related to the luminosity of the central source.

Key words: ISM: jets and outflows — ISM: kinematics and dynamics — ISM: molecules — masers — stars: formation

1. INTRODUCTION

Molecular outflow toward a high-mass young stellar object (YSO) was first detected in Orion A (Zuckerman et al. 1976; Kwan & Scoville 1976). In an early survey by Bally & Lada (1983), most of the objects were high-mass star-forming regions. However, the study of low-mass outflows advanced much more rapidly after the extended and collimated outflow in L1551 was detected (Snell et al. 1980). Until 1999, less than 30 massive outflows were cataloged (Churchwell 1999) when the total number of molecular outflows exceeded 200 (Wu et al. 1996). Efforts have been made to search for high-mass outflows in recent years (Beuther et al. 2002a; Zhang et al. 2001; Ridge & Moore 2001; Shepherd & Churchwell 1996a, 1996b). A large number of new outflows have been uncovered. Nevertheless, the search for outflows from massive YSOs is hindered by both the complexity of and the relatively large distances to these sources. In particular, massive YSOs are usually associated with a cluster of lower mass YSOs. The possibility of multiple outflow lobes complicates the identification.

Outflows are usually searched for with the easily excited CO $J = 1-0$ line. However, by observing lines at higher frequencies, one can attain higher angular resolution, which is critical to reduce the beam dilution and to identify relatively compact outflows. In addition, higher J transitions are relatively more sensitive to hot gas when the high-velocity gas is optically thin. Such hot gas are more likely to be physically associated with YSOs.

In this paper we present observations of the CO $J = 2-1$ line toward 11 high-mass star-forming regions. Four (OMC 2, GGD 27, G35.2–0.74, and IRAS 22543+6145) were selected from outflows measured with the CO $J = 1-0$ line (Wu et al. 1996 and references therein). The remaining were selected from outflow candidates detected in previous CO $J = 1-0$ surveys of massive star-forming regions or water maser sources (Wu et al. 1998a, 1998b). The sources and their references are listed in Table 1. We describe the observations in § 2. The results and discussions of the outflows and their driving sources are given in §§ 3 and 4. We summarize in § 5.

2. OBSERVATIONS

Observations of the CO $J = 2-1$ line were made with the 12 m telescope of NRAO⁵ during 1998 February 22–23. The beam size at this wavelength (230.53799 GHz) is about 29'',

¹ Department of Astronomy, CAS-PKU Joint Beijing Astrophysics Center, Peking University, Beijing 100871, China; yfwu@bac.pku.edu.cn.

² Harvard-Smithsonian Center for Astrophysics, 60 Garden Street, Cambridge, MA 02138; qzhang@cfa.harvard.edu.

³ Department of Astronomy and Steward Observatory, University of Arizona, Tucson, AZ 85721; hua_chen@net.com.

⁴ Department of Astronomy, Columbia University, New York, NY 10027; cyyang@astro.columbia.edu.

⁵ The National Radio Astronomy Observatory is a facility of the National Science Foundation operated under cooperative agreement by Associated Universities, Inc.

TABLE 1
OBSERVED SOURCES

Source Name (1)	R.A. (B1950) (2)	Decl. (B1950) (3)	D (kpc) (4)	H ₂ O (5)	CO $J = 1-0^a$ (6)	References (7)	V_{LSR} (km s ⁻¹) (8)	Bipolar Outflow (9)
OMC 2	05 32 59.6	-05 11 32	0.5	Y	O	1, 2	10.5	Y
GGD 27	18 16 13.0	-20 48 43	1.7	Y	O	1, 3	10.7	Y
IRAS 18314-0720	18 31 26.8	-07 20 29	6.1	Y	C	4	103.8	N
G35.2-0.74	18 55 41.0	01 36 32	2.0	Y	O	1, 5	32.7	N
IRAS 19209+1421	19 20 54.6	14 21 01	6.8	Y	...	6	46.7	N
S146	22 47 31.0	59 39 43	5.2	Y	O	4	-48.2	Y
IRAS 22506+5944	22 50 37.0	59 44 50	5.1	Y	C	4	-50.3	Y
IRAS 22543+6145	22 54 20.2	61 45 55	0.73	Y	O	1, 7	-11.6	Y
IRAS 23042+6000	23 04 14.9	60 00 04	5.2	N	C	8	-52.7	N
IRAS 23133+6050	23 13 21.5	60 50 47	5.8	N	C	8	-55.5	N
IRAS 23385+6053	23 38 30.2	60 53 41	4.7	Y	O	4	-49.6	Y

NOTE.—Units of right ascension are hours, minutes, and seconds, and units of declination are degrees, arcminutes, and arcseconds.

^a O and C indicate CO $J = 1-0$ outflow and outflow candidate, respectively.

REFERENCES.—(1) Wu et al. 1996; (2) Fischer et al. 1985; (3) Yamashita et al. 1989; (4) Wu et al. 1998a; (5) Dent et al. 1985; (6) Comoretto et al. 1990; (7) Ho et al. 1982; (8) Wu et al. 1998b.

and the pointing accuracy is 5''. The aperture efficiency η_{mb} is 32%. The eight beam array receiver was used, with system temperatures of about 700–1100 K. The hybrid spectrometer of 1536 channels was employed and was split into eight sections during the observation. Each section has 192 channels with a total bandwidth of 150 MHz. The equivalent velocity resolution is 1.02 km s⁻¹. The absolute position-switching mode was used. To avoid CO emission in the Galactic plane, we chose a reference position a few degrees off in Galactic latitude from the target source. Usually a clean CO offset position was found within two to three trials. The map sizes were typically about 5' × 5' and were extended to cover the line wing emissions. The grid spacing of the map is 29''. The integration time is 2 minutes for each position. The antenna temperature T_A^* has been corrected for atmospheric attenuation, radiation loss, and rearward and forward scattering and spillover. Data were reduced with the CLASS software.

To further identify the excitation sources of outflows, we observed 7 mm continuum emission in OMC 2 with the Very Large Array (VLA) of NRAO on 2001 September 30 in the compact D configuration. The pointing center of the observations was R.A.(B1950) = 05^h32^m59^s.58, decl.(B1950) = -05°11'40".4. We used the quasar 0539-057 to calibrate the time variations of gains. Taking advantage of the angular proximity of the calibrator and the target source, we used the fast-switching mode with a calibration duty cycle of 2 minutes. The rms in the image is about 0.2 mJy.

3. RESULTS

The results of outflow detection are summarized in Table 1. Columns (1)–(3) list the source names and the equatorial coordinates. Column (4) lists the distances, some of which are quoted from references, whereas others are calculated using the Galactic rotation model (Wouterloot & Brand 1989). Column (5) presents H₂O maser detection. Column (6) gives the results of the previous search for outflows in the CO $J = 1-0$ line. Column (7) lists the references. Column (8) presents the central velocities (V_{LSR}) of the CO $J = 2-1$ line. Column (9) gives the outflow detection in CO $J = 2-1$.

To identify CO outflows, we first examine whether there are high-velocity wings in the CO $J = 2-1$ spectra near the source positions and whether the intensities of the wing emission de-

crease smoothly toward the edge of the mapped region. In cases in which multiple velocity components are present, the wing emissions are likely from additional cloud components rather than from the high-velocity gas. The data are further examined in position-velocity (PV) diagrams for intervening cloud components. If confirmed, they should be excluded from the high-velocity emission. As a result, we found bipolar outflows in six sources. In the other five sources, including one previously identified as a bipolar outflow in CO $J = 1-0$, bipolar outflows cannot be confidently identified because of the confusion of multiple components. Sources are described in two groups in §§ 3.1 and 3.2. To analyze the properties of the YSOs in the region, we present in Table 2 the properties of the *IRAS* sources. The *IRAS* name, position, and the two color indexes are given in columns (2)–(6). The T_d in column (7) is the color temperature deduced from the 100 and 60 μ m flux densities. The infrared luminosity L_{FIR} in column (8) is calculated using

$$L_{\text{FIR}} \sim L_{5-1000 \mu\text{m}} = \pi D^2 1.75 \left(\frac{F_{12}}{0.79} + \frac{F_{25}}{2} + \frac{F_{60}}{3.9} + \frac{F_{100}}{9.9} \right)$$

(Casoli et al. 1986). To identify driving sources, we make use of the Two Micron All Sky Survey (2MASS) and other near-infrared data. The 7 mm map of OMC 2 from the VLA is presented. The possible driving sources are presented in Table 3.

3.1. Sources with Outflows

For each outflow source we present typical CO spectra with the blue- and redshifted emission. We determine the velocity ranges of high-velocity gas emission from PV diagrams. The PV diagram was drawn with a cut along the direction where the CO lines have the largest wings. We choose the beginning of the high-velocity wings at the value at which a velocity gradient clearly begins and is spatially extended. With PV diagrams, we can also identify additional velocity components (see § 3.2). For OMC 2 and GGD 27, we adopted the velocity ranges of CO $J = 1-0$ that have been confirmed by the PV diagram (Fischer et al. 1985; Yamashita et al. 1989; note that for GGD 27 there is a 2 km s⁻¹ systematic difference between the measured V_{LSR} of Yamashita et al. and this work).

For IRAS 22543+6145, the CO $J = 1-0$ outflow was measured by Rodríguez et al. (1980a). They adopted the high-velocity ranges as -60 to -21 km s⁻¹ and -1 to 14 km s⁻¹ for

TABLE 2
INFRARED PARAMETERS

Name (1)	IRAS Source (2)	Position ^a (s) (3)	Position ^a (arcsec) (4)	$\log(F_{25}/F_{12})$ (5)	$\log(F_{60}/F_{12})$ (6)	T_d (K) (7)	L_{FIR} (L_{\odot}) (8)
OMC 2	05329-0508	54.9	53	1.81	2.88	740	1.3×10^2
	05329-0512	58.7	11	0.38	1.44	^b	3.0×10^2
GGD 27.....	18162-2048	12.8	51	1.13	2.03	41	2.0×10^4
IRAS 18314-0720	18314-0720	26.8	29	0.62	1.48	37	5.2×10^5
G35.2-0.74.....	18556+0139	39.6	47	-0.23	0.69	21	5.7×10^2
	18556+0136	41.2	28	1.71	2.66	64	1.6×10^4
IRAS 19209+1421	19209+1421	54.6	01	1.00	2.06	32	7.7×10^5
	19209+1418	57.7	28	1.57	0.23	10	3.8×10^5
S146	22475+5939	30.9	03	0.78	1.52	42	6.2×10^4
IRAS 22506+5944	22506+5944	38.7	58	0.74	1.47	39	1.5×10^4
IRAS 22543+6145	22543+6145	20.2	55	1.86	3.06	38	1.7×10^4
IRAS 23042+6000	23042+6000	14.9	04	0.55	1.56	38	4.0×10^4
IRAS 23133+6050	23133+6050	21.5	47	1.11	1.67	42	2.1×10^5
IRAS 23385+6053	23385+6053	30.1	43	0.54	1.84	32	2.4×10^4

^a For an *IRAS* source, HHMMS±DDAA, its position is R.A. = HH^hMM^mss^s, decl. = DD^oAA'aa'', where ss.s is the value in column (3) and aa is the value in col. (4).

^b A physically meaningful temperature cannot be derived when $F_{60} > (5/3)^4 F_{100}$ ($\beta = 1$).

blue and red wings, respectively. Ho et al. (1982) analyzed the outflow gas with $V < -16.9 \text{ km s}^{-1}$ and $V > -5.1 \text{ km s}^{-1}$ for blue and red wings, respectively. The CO lines have prominent absorption at the line center. We have made channel maps to examine how the high-velocity gas is distributed from close to the line center to the line wing. The emission integrated within -6 to -3 km s^{-1} appears to show an additional component to the south of the red lobe. We checked the spectra and found that this velocity range coincides with the absorption. Thus, this component is probably not real but is due to absorption. We define the high-velocity range as $V < -16 \text{ km s}^{-1}$ for the blue wing and $V > -3 \text{ km s}^{-1}$ for the red wing to avoid the self-absorption. Our high-velocity ranges are closer to the line center than those of Rodríguez et al. (1980a). All the velocity ranges of bipolar outflows are indicated in the CO spectrum in panel (a) and the PV diagrams in panel (b) of the corresponding outflow figures.

The outflow parameters were calculated following the procedure of Garden et al. (1991). Assuming LTE and optically thin emission in the CO gas, the column density of CO is given by

$$N_{\text{CO}} = \frac{1.1 \times 10^{13} (T_{\text{ex}} + 0.93) \exp(5.5/T_{\text{ex}}) \int T_R(\text{CO}) dV}{[J_{\nu}(T_{\text{ex}}) - J_{\nu}(T_{\text{bg}})][1 - \exp(-11.1/T_{\text{ex}})]} \text{ cm}^{-2},$$

where $J_{\nu}(T)$ is the Planck function and $\int T_R(\text{CO}) dV$ is the integrated intensity of the high-velocity CO $J = 2-1$ emission in units of K km s^{-1} . A number of studies show that high-velocity gas is usually optically thick (Goldsmith et al. 1984; Snell et al. 1984; Shepherd & Churchwell 1996b).

The effect of the optical depth on the mass estimation is complex. It is better to adopt a velocity-dependent τ (see Arce & Goodman 2001; Yu et al. 1999). So far the majority of authors have used constant values of τ for one or two velocity ranges, respectively. The average value for different sources or the entire line wing is usually around 4 (e.g., Snell et al. 1984; Goldsmith et al. 1984; Garden et al. 1991). Occasionally, $\tau = 1$ or 5 was used to see the effect of the optical depth on mass estimation (Shepherd & Churchwell 1996a; Chernin & Masson 1991). Thus, our optically thin assumption would produce a lower limit on the mass.

The expression T_{ex} is the excitation temperature in Kelvin. It changes with velocity and position, but using a proper constant T_{ex} affects little the estimated total mass (Arce & Goodman 2002). Generally speaking, T_{ex} in low-mass star-forming regions is about 10 K (Goldsmith et al. 1984), but about 30 K where high-mass stars form (Shepherd & Churchwell 1996a, 1996b).

We adopted T_d , which is calculated using *IRAS* flux density at 60 and 100 μm and adopting a power law with index 2 for the dependence of dust opacity on the frequency. The dust temperature T_d is usually larger than the gas temperature by as much as 10 K (Wu & Evans 1989). This difference would produce 30% uncertainty in the estimated column density. With the above procedure, the mass estimated is expected to be 3 times larger. For OMC 2, the value of T_d is not physically meaningful, and the main-beam brightness temperature $T_{\text{mb}} = T_R^*/\eta_{\text{mb}}$ of the CO line is used. If we take $[\text{CO}]/[\text{H}_2] = 10^{-4}$ and the mean atomic weight of the gas $\mu_g = 1.36$ to account for helium, the total mass M of the outflow gas can be estimated. The momentum P and energy E are proportional to $\Sigma \int T(v)v dv$ and $\Sigma \int T(v)v^2 dv$, respectively, where v is the velocity of the gas relative to the cloud systemic velocity. The dynamical timescale t is estimated as R/V , where R is assumed to be the mean distance from the peaks of the blueshifted and redshifted gas to the identified driving source. The expression V is the characteristic velocity derived from $V = P/M$ (Lada 1985). The mechanical luminosity is $L = E/t$, and the driving force is $F = P/t$. The mass-loss rate is $\dot{M} = P/(tV_w)$, where the wind velocity V_w is assumed to be 500 km s^{-1} (Marti et al. 1998). The outflow parameters we obtained for the six outflow sources are listed in Table 4.

In the following, we discuss the sources individually.

OMC 2.—It is located in the north of the Trapezium OB star cluster. A cluster of low- to intermediate-mass pre-main-sequence stars is seen in the near-infrared image. The compact near-infrared sources IRS 1, 2, 3, and 4N are the illuminating sources of the reflection nebulae (Rayner et al. 1989). IRS 4N (near the reference position, indicated as an open triangle in Fig. 1c) is associated with the H_2 S(1) line emission (Fischer et al. 1980). Wang (1997) also detected an H_2 jet originating

TABLE 3
DRIVING SOURCE IDENTIFIED

Source	2MASS Source	Other Near-Infrared Source	IRAS	Millimeter Continuum	Centimeter Continuum	References
OMC 2	05352763–0509371 ^a	IRS 4N	...	7, 1.3	3.6	1, 2, 3
GGD 27	18191220–2047297	IRS 2	18162–2048	...	2, 3.6, 6	4, 5, 6
S146	22492900+5954560	132	22475+5939	...	6	7, 8, 9
IRAS 22506+5944	22523871+6000445	83	22506+5944 ^a	7
IRAS 22543+6145	22561976+6201509	HW 2	22543+6154 ^a	...	3.6	5, 10
IRAS 23385+6053	23405396+6110421	...	23385+6053 ^b	3.4	6	11, 12

^a There are two 2MASS sources within its error ellipse.

^b The deviation between the IRAS and the 2MASS source is $\sim 21''$.

REFERENCES.—(1) Rayner et al. 1989; (2) this paper; (3) Reipurth et al. 1999; (4) Yamashita et al. 1987; (5) Kurtz et al. 1994; (6) Rodríguez & Reipurth 1989; (7) Wang 1997; (8) Felli & Harten 1981; (9) Felli et al. 1978; (10) Hughes & Wouterloot 1984; (11) Molinari et al. 1998; (12) Gregory & Condon 1991.

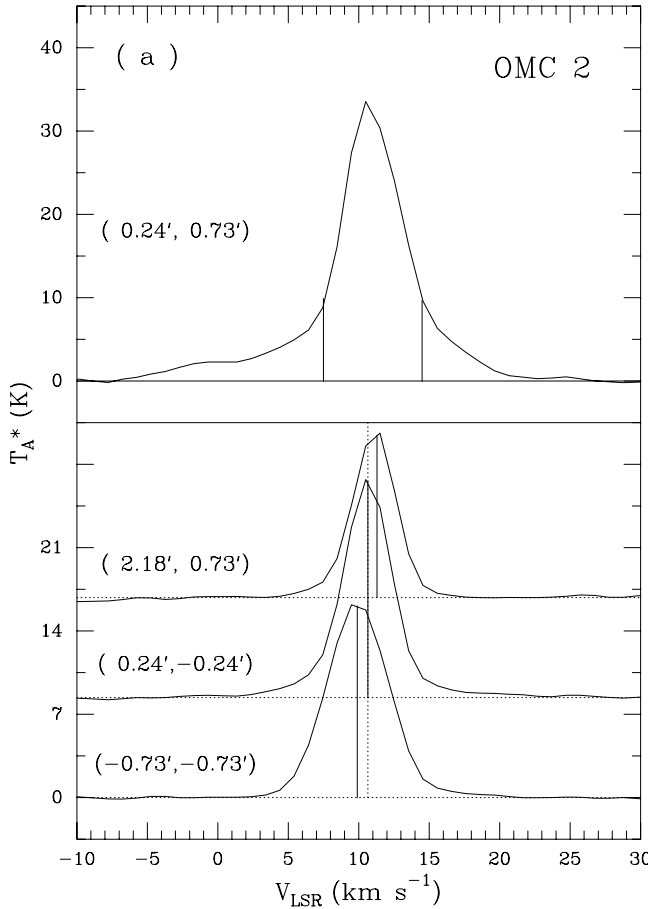


FIG. 1a

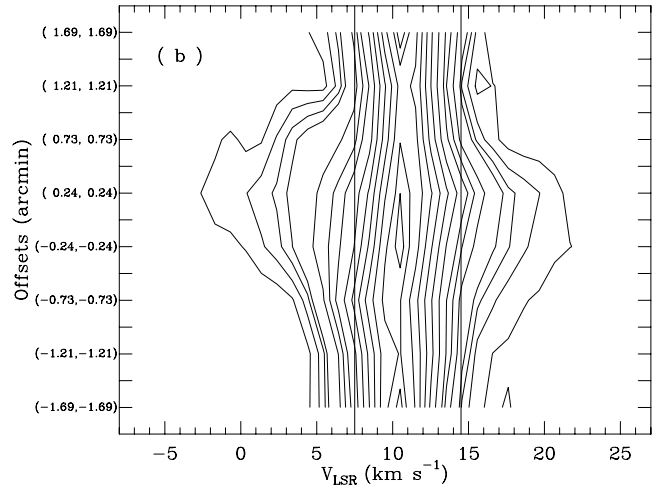


FIG. 1b

FIG. 1.—Figures for OMC 2. (a) Spectra. The left and right vertical lines in the top panel indicate the beginning of the blue and red wings, respectively. The bottom panel shows the line velocity shifts. (b) PV diagram. Contour levels are 0.5 to 2.0 K by 0.5 K, 4.0 to 12.0 K by 2.0 K, and 16.0 to 36.0 K by 4.0 K; the vertical lines show the same velocity values as those in (a). (c) Contour map of the wing emissions (line-center velocity shifts corrected), integrated over about -7.5 to 7.5 km s^{-1} for the blue wing (solid line) and about 14.5 – 26.5 km s^{-1} for the red wing (dashed line), respectively. The cross denotes the reference position for the relative coordinates (IRS 4). The filled triangles mark the locations of IRAS sources. Small crosses are the observed points. Contours begin from 17.0 K km s^{-1} with increasing steps of 4.2 K km s^{-1} for the blue wing and begin from 11.7 K km s^{-1} with increasing steps of 2.9 K km s^{-1} for the red wing. The H_2 jet detected by Wang (1997) was superposed on our outflow lobes. (d) VLA map at 7 mm continuum emission. Contours are $-3, -2, -1, 1, 2, 3, 4, 5, 6, 7, 8$, and 10×0.6 mJy beam^{-1} . The circle at the bottom left corner marks the synthesized beam.

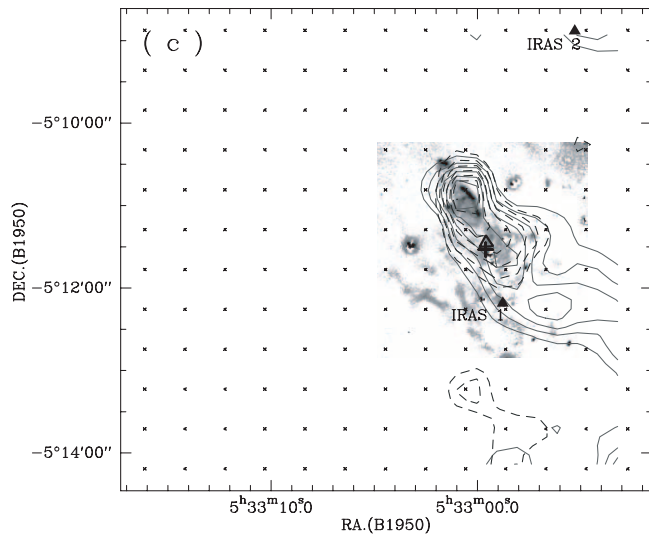


FIG. 1c

from IRAS 4N. IRAS 05329–0512, labeled as IRAS 1 in the map (Fig. 1c), is located near IRS 3. Another *IRAS* source, IRAS 05329–0508 (labeled as IRAS 2 in the map), is 3.5' north and located at the edge of the map. Two H₂O masers were detected in this region (Tofani et al. 1995). Fischer et al. (1985) detected an outflow in the CO $J = 1-0$ line, and the blue and the red lobes overlap considerably. We present in the top panel of Figure 1a a CO $J = 2-1$ spectrum taken from near the position of IRS 4N. The line exhibits a large velocity extent (−7.5 to −26.5 km s^{−1}, measured at the 0.2 K level). The spectra in the bottom panels are taken from different positions and show a shift in line-center velocities. A PV diagram is shown in Figure 1b. The cut is along the outflow axis and through the position of IRS 4N. The boundary between the high-velocity gas and the ambient gas and the different spatial distribution of the blue wing and the red wing can be clearly seen. Figure 1c shows contours of the blue- and the redshifted gas emission. The H₂ jet detected by Wang (1997) was superposed on our outflow lobes. From the near-infrared image, one can see clearly a bow shock pointing to the northeast direction (Wang 1997). It is consistent with the morphology of the molecular outflow.

The near-infrared source IRS 4N is identified to be the driving source for the OMC 2 outflow by Rayner et al. (1989). It is located nearly on the axis of the CO outflow and the H₂ jet (Wang 1997). To further investigate the driving source, we observed 7 mm continuum emission with VLA. We found that a compact structure almost coincides with IRS 4N. The 7 mm source corresponds to VLA 11 (Reipurth et al. 1999). It shows the existence of thermal emission there and confirms IRS 4N as the driving source. We use the flux density of the *IRAS* source to estimate the bolometric luminosity of the driving source.

GGD 27.—This is an infrared reflection nebulosity (Hartigan & Lada 1985). There are at least three stellar sources in this region, of which IRS 2 is the illuminating source (Yamashita et al. 1987). There is only one *IRAS* source, IRAS 18162–2048, within the map, which corresponds to IRS 2. A water maser was found near GGD 27 by Rodríguez et al. (1980b). A bipolar molecular outflow was detected in CO $J = 1-0$ by Yamashita et al. (1989). Our CO $J = 2-1$ results are shown in Figure 2. The total velocity width at zero intensity for CO $J = 2-1$ at (−0.24, 0.24) is 46 (from −6 to 40) km s^{−1}, which is larger than that of CO $J = 1-0$ at the same rms level. In the bottom panel of

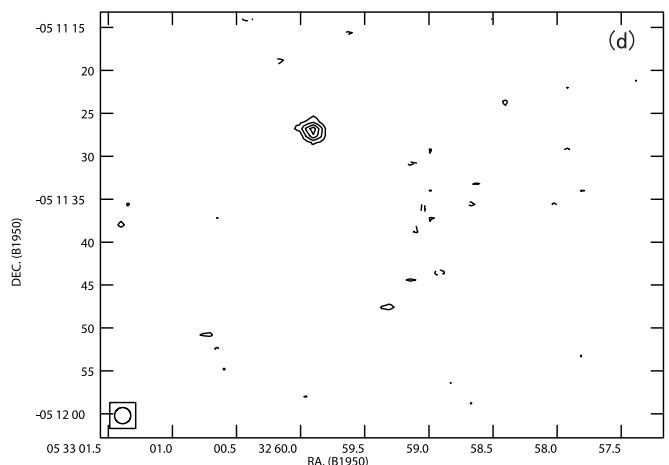


FIG. 1d

Figure 2a, we present two spectra showing shifts in line velocity. Figure 2b presents the PV diagram. The boundary between the outflow and the core material is clear. Comparing with the diagram in Yamashita et al. (1989), one can see that the CO $J = 2-1$ line has wings that extend further in velocity than those of the CO $J = 1-0$ line. The spatial extent of the wing emission is smaller. The distribution of the blue- and redshifted gas is presented in Figure 2c. The total mass in the flow obtained in this paper is $27 M_{\odot}$, much less than the $460 M_{\odot}$ obtained by Yamashita et al. (1989) from CO $J = 1-0$. In estimating outflow mass from CO $J = 1-0$, Yamashita et al. used optical depths of 4.4–6.8 for each lobe.

IRS 2 and IRAS 18162–2048 are located near the flow axis and are shown as open and filled triangles, respectively. The *IRAS* source has colors satisfying the criteria of the ultracompact (UC) H II regions (Wood & Churchwell 1989) and a large FIR luminosity. At its position, continuum emission at 6 cm was detected by Rodríguez & Reipurth (1989). The image of the 6 cm continuum was superposed on the flow. Kurtz et al. (1994) imaged the UC H II region at 2.0 and 3.6 cm and reported a radio source G10.841–2.592 at α (B1950) = 18^h16^m13^s, δ (B1950) = −20°48'48".7. These observations confirm that IRS 2 is the driving source of the outflow.

The corresponding 2MASS source 18191220–2047297 is at α (B1950) = 18^h16^m13^s17, δ (B1950) = −20°48'47".08 and is 16.267, 13.155, and 9.674 mag at the *J*, *H*, and *K_s* bands, respectively.

S146.—This is an H II region with weak H α emission (Blair et al. 1975). H₂O maser emission with multiple components has been detected (Blair et al. 1978; Henkel et al. 1986). Both the optical and the 6 cm images show a bipolar structure (Felli & Harten 1981). Mapping in the CO $J = 1-0$ line shows a bipolar outflow (Yang & Wu 1998). The CO $J = 2-1$ spectra in Figure 3 show asymmetric line profiles and broad wings (see the top panels of Fig. 3a). The PV diagram with a cut along the outflow axis in the north-south direction (Fig. 3b) shows the high-velocity outflow. The contours of the wing emission in Figure 3c show that the blue lobe and the red lobe overlap. The peaks of the two lobes are about 40'' apart. The total line width in CO $J = 2-1$ (−60 to −35 km s^{−1}) is larger than that of CO $J = 1-0$ (−57.5 to −41.5 km s^{−1}; Yang & Wu 1998). Wang (1997) imaged this region in the *J*, *H*, and *K* bands.

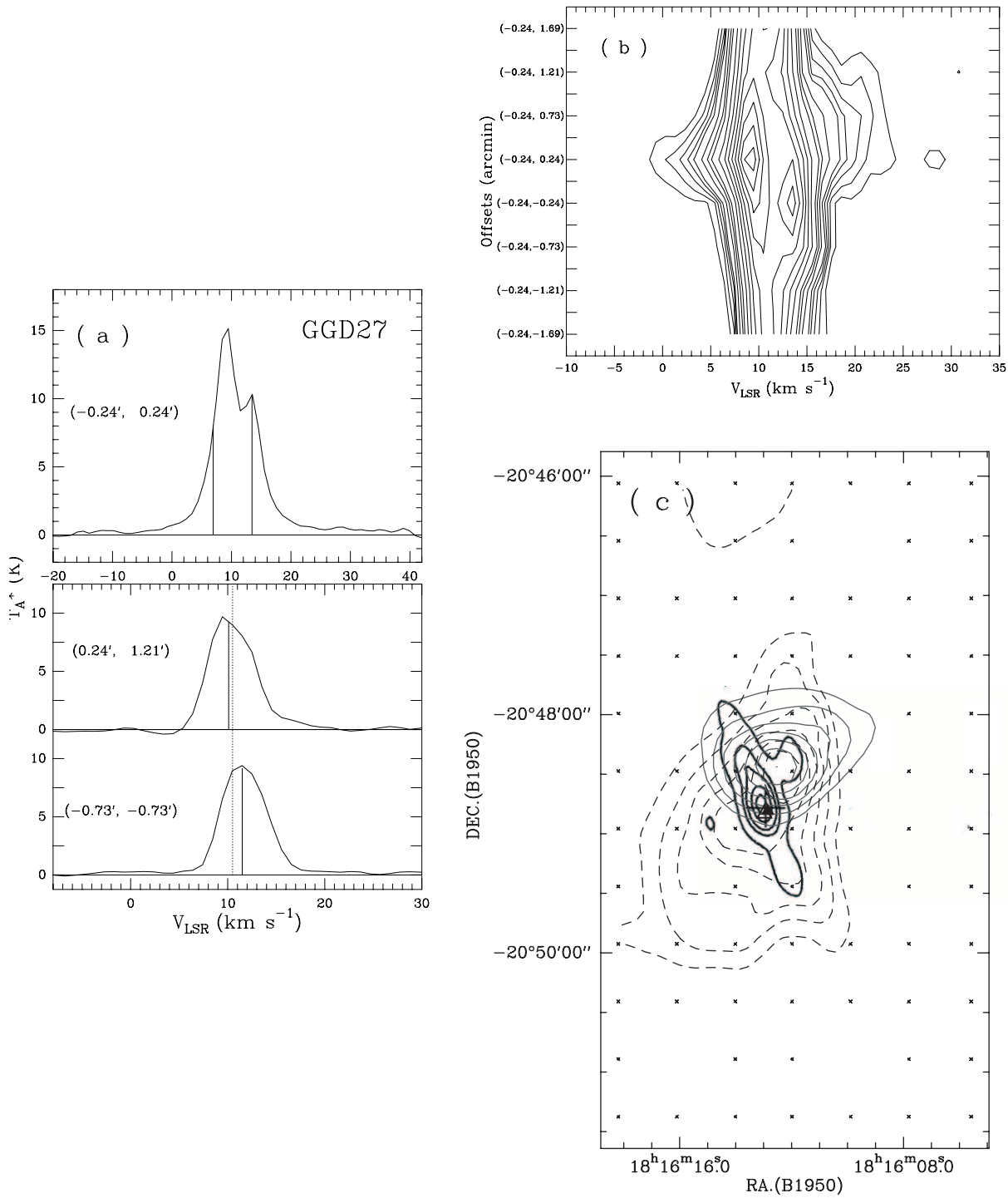


FIG. 2.—Figures for GGD 27. (a) Spectra. The left and right vertical lines in the top panel indicate the beginning of the blue and red wings, respectively. The bottom panel shows the line velocity shifts. (b) PV diagram. Contour levels are from 0.5 to 1.5 K by 0.25 K, 2.1 to 4.8 K by 0.5 K, and 6.2 to 14.4 K by 1.3 K; the vertical lines show the same velocity values as those in (a). (c) Contour map of the wing emissions, integrated over -7.4 to 8.5 km s^{-1} for the blue wing (solid line) and 12.5 to 40.0 km s^{-1} for the red wing (dashed line), respectively. The filled triangle marks the *IRAS* source position (the reference position). Contours begin from 16.1 K km s^{-1} with increasing steps of 4.0 K km s^{-1} for the blue wing and begin from 18.5 K km s^{-1} with increasing steps of 4.5 K km s^{-1} for the red wing. The thick lines present the 6 cm image of the excitation source (Rodriguez & Reipurth 1989).

Number 132 in Wang's near-infrared source list [at $\alpha(\text{B1950}) = 22^{\text{h}}47^{\text{m}}30^{\text{s}}.4$, $\delta(\text{B1950}) = 59^{\circ}39'01''.5$] is close to the flow axis and the red peak and is indicated as an open triangle in Figure 3c. It is also the brightest source (12.4, 11.2, and 10.1 mag at the *J*, *H*, and *K* bands, respectively) near the flow peak. The corresponding 2MASS source 22492900+5954560 is at

$\alpha(\text{B1950}) = 22^{\text{h}}47^{\text{m}}30^{\text{s}}.49$, $\delta(\text{B1950}) = 59^{\circ}39'02''.13$ and with 12.946, 11.410, and 10.407 mag at the *J*, *H*, and *K*_s bands, respectively. The positions and near-infrared magnitudes detected by Wang (1997) and 2MASS are consistent. The IR source coincides with IRAS 22475+5939 and the 6 cm emission peak (Felli et al. 1978). The L_{bol} of the *IRAS* source is $6.2 \times 10^4 L_{\odot}$ at a

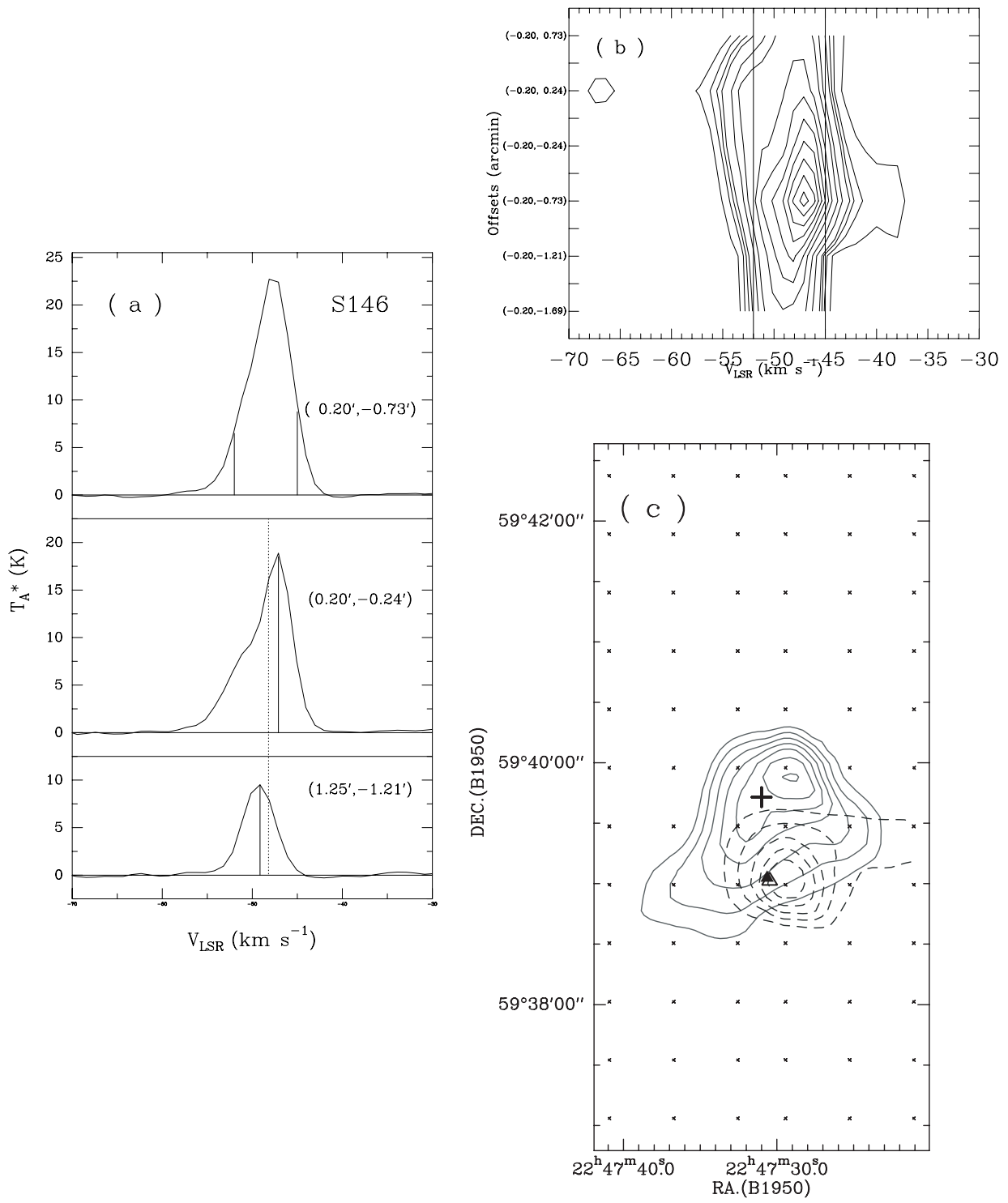


FIG. 3.—Figures for S146. (a) Spectra. The left and right vertical lines in the top panel indicate the beginning of the blue and red wings, respectively. The bottom panel shows the line velocity shifts. (b) PV diagram. Contour levels are from 0.5 to 1.5 K by 0.5 K, 2.0 to 5.0 K by 1.5 K, and 7.5 to 21 K by 2 K; the vertical lines show the same velocity values as those in (a). (c) Contour map of the wing emissions, integrated over -60.0 to -52.0 km s^{-1} for the blue wing (solid line) and -45.0 to -35.0 km s^{-1} for the red wing (dashed line), respectively. Contours begin at 6.5 K km s^{-1} with increasing steps of 2.0 K km s^{-1} for the blue wing and begin at 7.5 K km s^{-1} with increasing steps of 2.4 K km s^{-1} for the red wing. The open triangle denotes near-infrared source number 132 in the list of Wang (1997).

distance of 5.2 kpc. A star with spectral type O6.5 or earlier is needed to account for the ionization of the H II region and the infrared radiation (Felli & Harten 1981). This source is likely to be responsible for the driving of the outflow.

IRAS 22506+5944.—This source was named 10860+0049 (Comoretto et al. 1990). It is located beyond the solar circle.

Strong water maser emission has been detected with multiple velocity components (Wouterloot & Walmsley 1986; Comoretto et al. 1990). VLA observations show that there are three masers in this region (Jenness et al. 1995). The CO $J = 1-0$ line shows two components at -51.0 and -9.29 km s^{-1} (Wouterloot & Brand 1989). Wu et al. (1998a) measured the CO $J = 1-0$ line width at

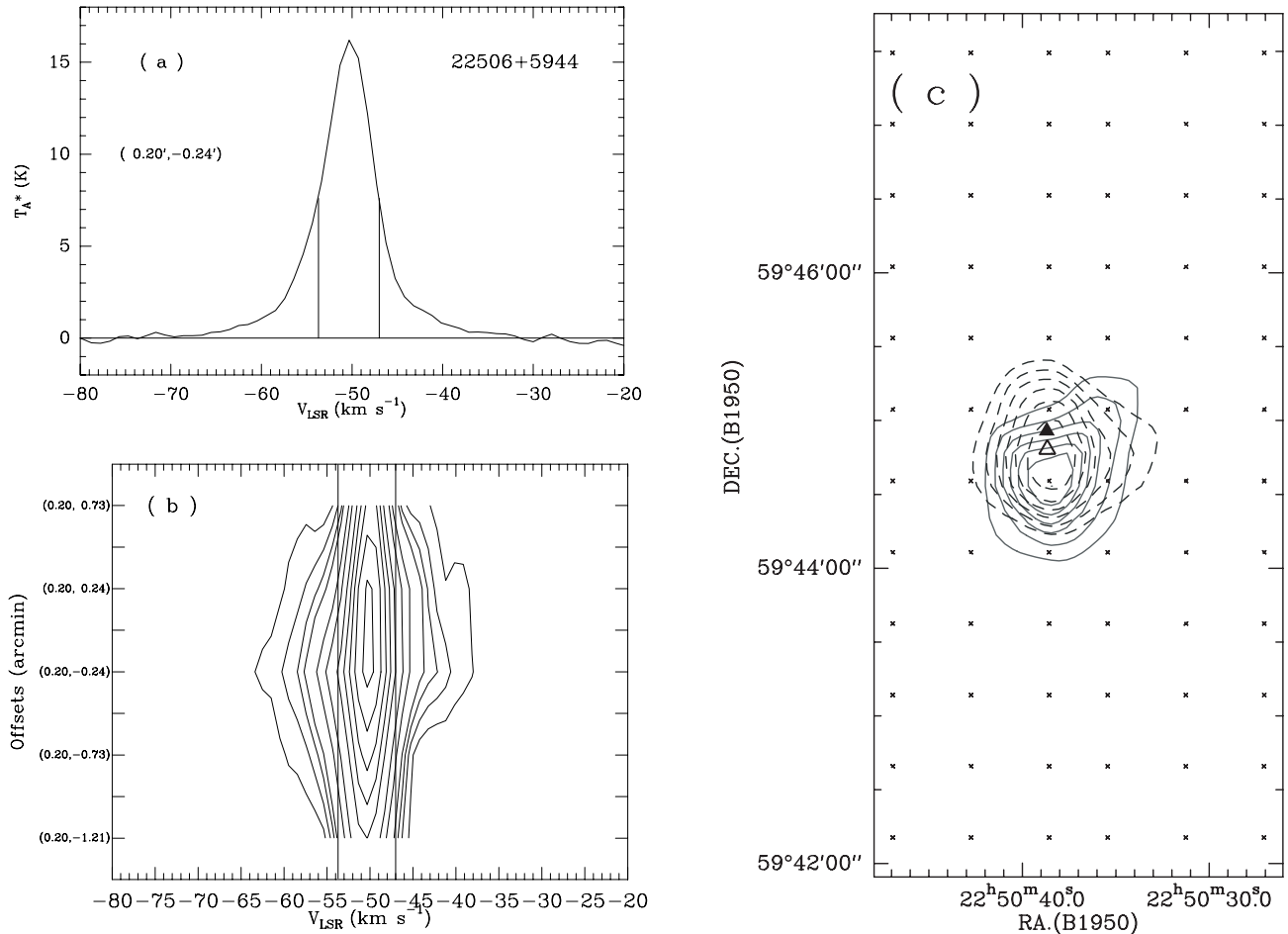


FIG. 4.—Figures for IRAS 22506+5944. (a) Spectrum. The left and right vertical lines indicate the beginning of the blue and red wings, respectively. (b) PV diagram. Contour levels are 0.5 to 1.5 K by 0.5 K, 2.0 to 5.0 K by 1.5 K, and 7.5 to 21 K by 2 K; the vertical lines show the same velocity values as in (a). (c) Contour map of the wing emissions, integrated over -69.3 to -53.7 km s^{-1} for the blue wing (solid line) and -47.0 to -31.7 km s^{-1} for the red wing (dashed line), respectively. Contours begin at 12.7 K km s^{-1} with increasing steps of 3.1 K km s^{-1} for the blue wing and begin at 11.5 K km s^{-1} with increasing steps of 2.9 K km s^{-1} for the red wing. The filled triangle marks the locations of the *IRAS* source. Small crosses are the observed points. The open triangle denotes the near-infrared source S4 (number 83) detected by Wang (1997).

zero intensity to be 15.1 km s^{-1} . The CO $J = 2-1$ spectrum shown in Figure 4a is taken at $(\Delta\alpha, \Delta\delta) = (0'.20, -0'.24)$ from the reference position. The total line width at zero intensity is about 35 km s^{-1} . The PV diagram (Fig. 4b) with a cut along the north-south direction shows high-velocity wings. The contour map of the blue- and redshifted gas in Figure 4c shows that the two lobes largely overlap. Two of the three masers are also located close to the flow peak position (Jenness et al. 1995). Wang (1997) imaged the source in the near-infrared J , H , and K bands and found a cluster within the cloud core. The one labeled S4 (number 83 in Wang's near-infrared photometry list) resides at $\alpha(\text{B1950}) = 22^{\text{h}}50^{\text{m}}38^{\text{s}}85$, $\delta(\text{B1950}) = 59^{\circ}44'46''.6$, close to the peak of the outflow, which is presented as an open triangle in Figure 4c. It has magnitudes of 17.7, 14.5, and 11.7 in the J , H , and K bands, respectively (Wang 1997). It corresponds to a 2MASS source, 22523871+6000445, at $\alpha(\text{B1950}) = 22^{\text{h}}50^{\text{m}}38^{\text{s}}83$, $\delta(\text{B1950}) = 59^{\circ}44'46''.49$ with 16.306, 13.449, and 10.950 mag in the J , H , and K_s bands, respectively. S4 is closer to the flow center and is likely to be the driving source. It also coincides with IRAS 22506+5944. The *IRAS* source has a luminosity of $1.5 \times 10^4 L_{\odot}$ at a distance of 5.1 kpc. Its colors satisfy the UC H II region criteria (Wood & Churchwell 1989). The bolometric luminosity of IRAS 22506+5944 is taken as the luminosity of the driving source in the following analysis.

IRAS 22543+6145.—The outflow in Cep A is one of the first outflows discovered (Rodríguez et al. 1980a; Ho et al. 1982). It has been mapped in both the CO $J = 1-0$ line and later in the CO $J = 3-2$ line (Narayanan & Walker 1996; Choi et al. 1993). A strong water maser exists in this source (Wu et al. 1999; Comoretto et al. 1990 and references therein). The results in the CO $J = 2-1$ line are shown in Figure 5. The spectra in Figure 5a are taken from three positions. The blue wing extends to -40 km s^{-1} and the red one to 21.6 km s^{-1} . It appears that the line profiles are relatively complex and there are dips in the line center. Based on the variation of the line profiles from the edge to the center of the map, we think that the peak at about -11.5 km s^{-1} is the counterpart of the component in the edge region. The peak agrees well with the CS $J = 7-6$ observation (-12 km s^{-1} ; Narayanan & Walker 1996) and represents the ambient gas. The velocity variations of this peak contain an east-west component and a north-south component. The velocity increases about 2 km s^{-1} in a region of $2'.5$ along the northeast to southwest direction (shown in Fig. 5a). The velocity shifts agree in general with the CS line measurements of Narayanan & Walker (1996). Figure 5b shows the PV diagram along the outflow axis (east-west direction). The spatial separation of the blue and the red wing is apparent. Figure 5c presents the contours of the high-velocity gas emissions. The

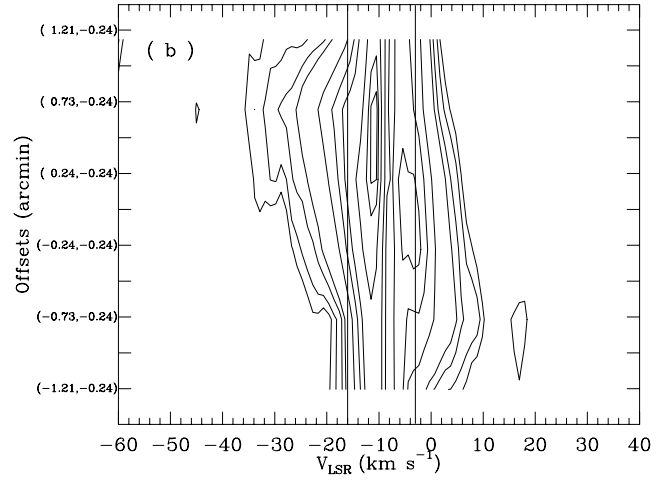


FIG. 5b

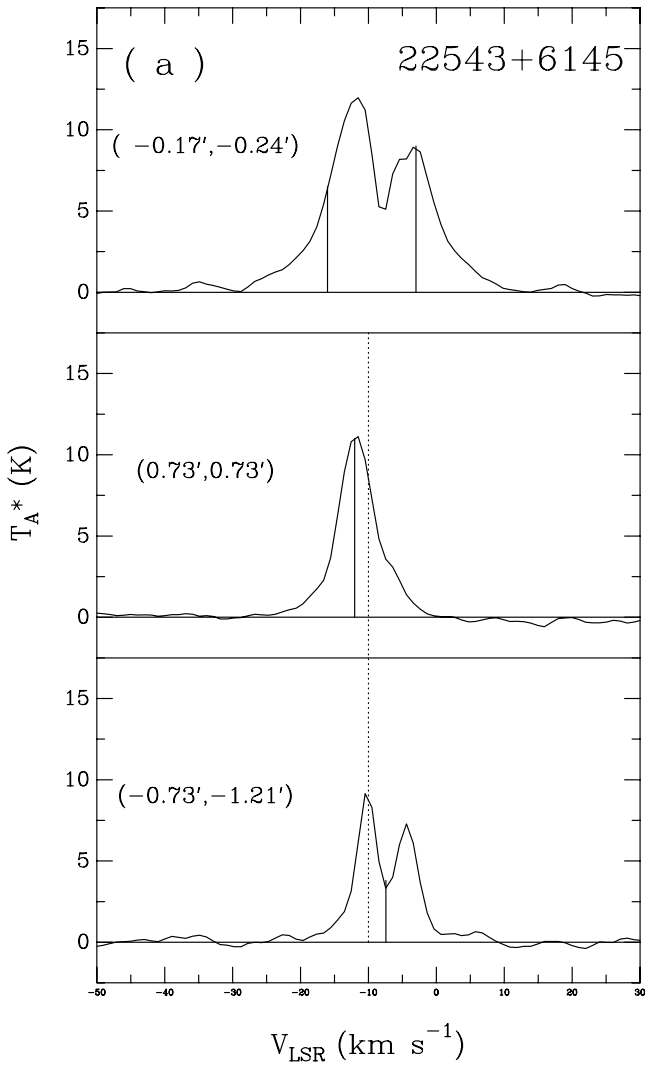


FIG. 5a

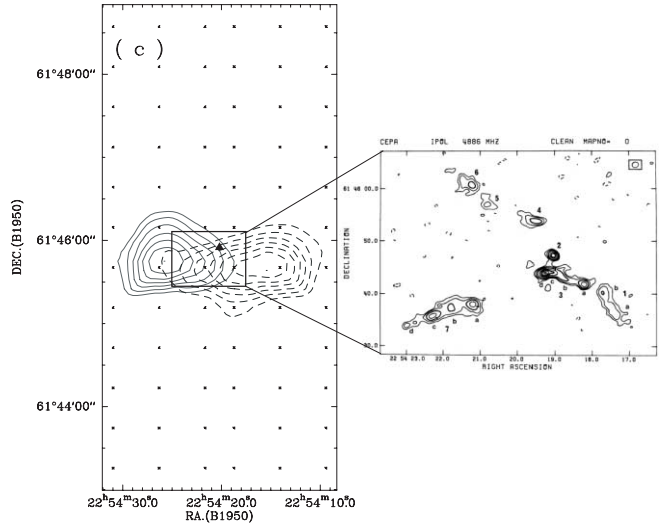


FIG. 5c

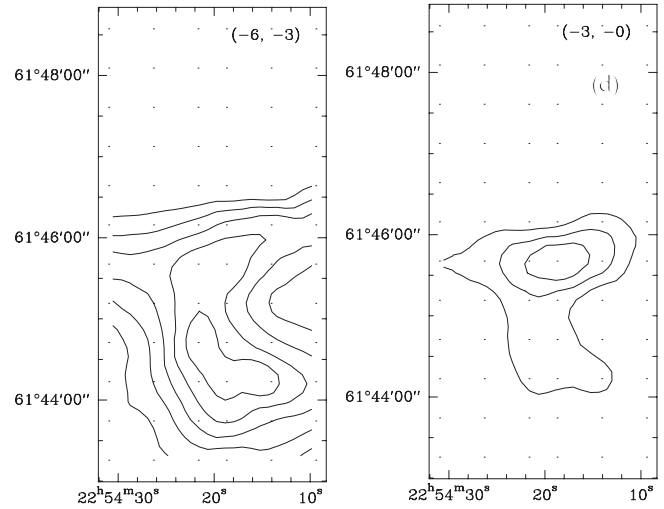


FIG. 5d

FIG. 5.—Figures for IRAS 22543+6145. (a) Spectra. The left and right vertical lines in the top panel indicate the beginning of the blue and red wings, respectively; the bottom panel shows the line velocity shifts. (b) PV diagram. Contour levels are 0.7, 1.0, 1.5, 2.0, 4.0, 6.0, 8.0, 11.0, 13.0, and 14 K; the vertical lines show the same velocity values as those in (a). (c; left) Contour map of the wing emissions, integrated over -40.0 to -16.0 km s^{-1} for the blue wing (solid line) and -3.0 to 21.6 km s^{-1} for the red wing (dashed line), respectively. Contours begin at 27.2 K km s^{-1} with increasing steps of 6.8 K km s^{-1} for the blue wing and begin at 20.3 K km s^{-1} with increasing steps of 5.1 K km s^{-1} for the red wing. (Right) The 6 cm continuum image of HW 2 (Hughes & Wouterloot 1984). (d) Channel maps of velocity ranges $(-6, -3)$ km s^{-1} (left) and $(-3, 0)$ km s^{-1} (right). Contour levels are from 10 to 26 K by 4 K .

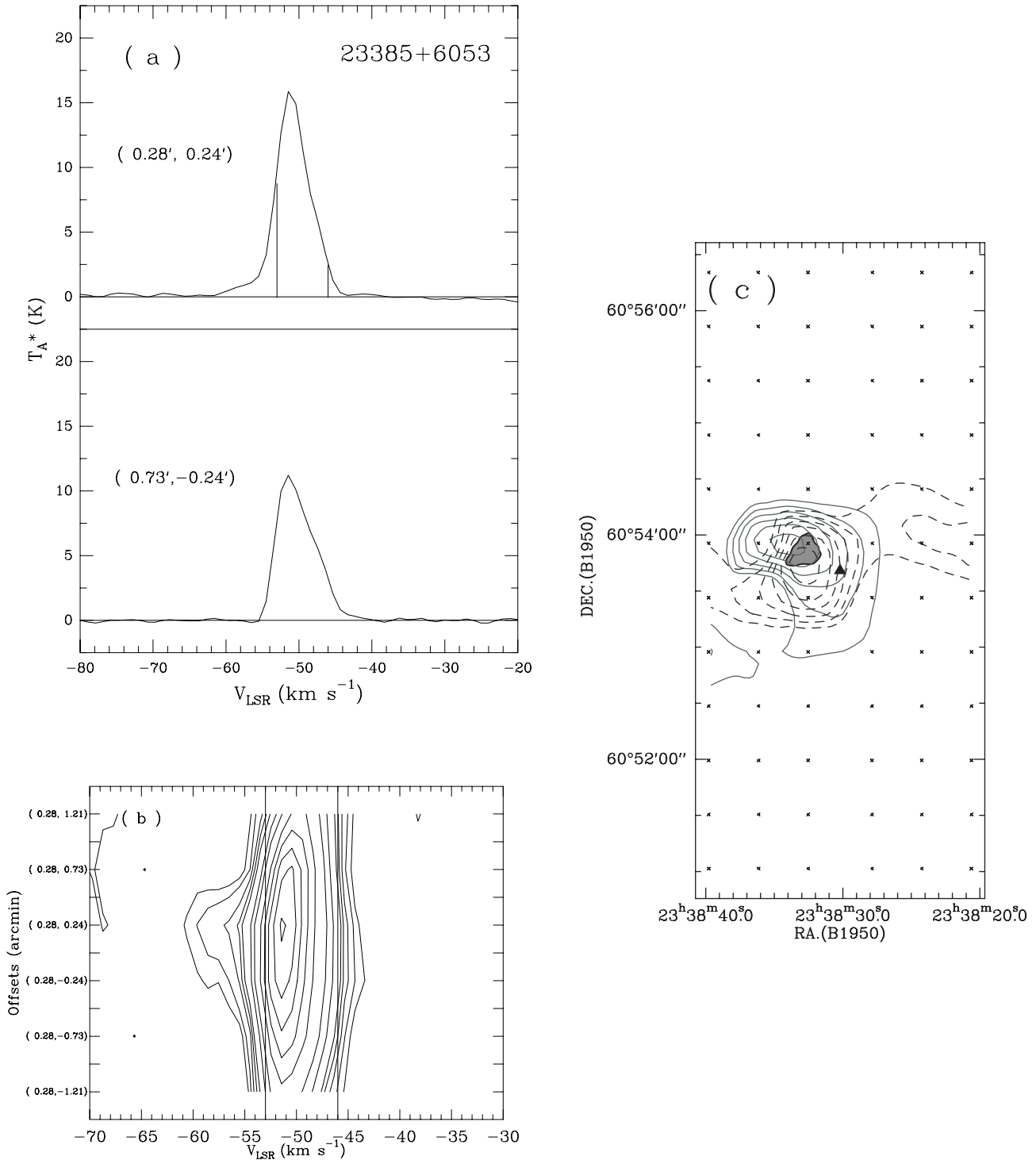


FIG. 6.—Figures for IRAS 23385+6053. (a) Spectra. The left and right vertical lines indicate the beginning of the blue and red wings, respectively. (b) PV diagram. Contour levels are 0.25 K, 0.5 to 1.5 K by 0.5 K, 2.0 to 5.0 K by 1.5 K, and 7.5 to 21 K by 2 K; the vertical lines show the same velocity values as those in (a). (c) Contour map of the wing emissions, integrated over -61.7 and -53.4 km s $^{-1}$ for the blue wing (solid line) and -46.1 to -41.8 km s $^{-1}$ for the red wing (dashed line), respectively. Contours begin at 4.6 K km s $^{-1}$ with increasing steps of 1.0 K km s $^{-1}$ for the blue wing and begin at 7.5 K km s $^{-1}$ with increasing steps of 1.2 K km s $^{-1}$ for the red wing. The 3.4 mm emission image is superposed on the contours as a shaded region (Molinari et al. 1998).

outflow mass we computed is similar to that of CO $J=1-0$, considering the different ratio of $^{12}\text{CO}/\text{H}_2$ (Rodríguez et al. 1980a). HW 2 was identified as the driving source of the outflow (Hughes & Wouterloot 1984; Narayanan & Walker 1996; Torrelles et al. 1998). Its 6 cm continuum image is indicated in the outflow map in Figure 5c (Hughes & Wouterloot 1984). The 2MASS source 22561976+6201509 [α (B1950) =

$22^{\text{h}}54^{\text{m}}20.873$, δ (B1950) = $61^{\circ}45'48.23''$] coincides with HW 2. Its magnitudes in the J , H , and K_s bands are 14.816, 12.338, and 8.640, respectively. HW 2 is located between the peaks of the blue and the red lobes and on the outflow axis, suggesting that it drives the outflow.

IRAS 23385+6053.—This H_2O maser source (Comoretto et al. 1990) was found to have an asymmetric line profile and

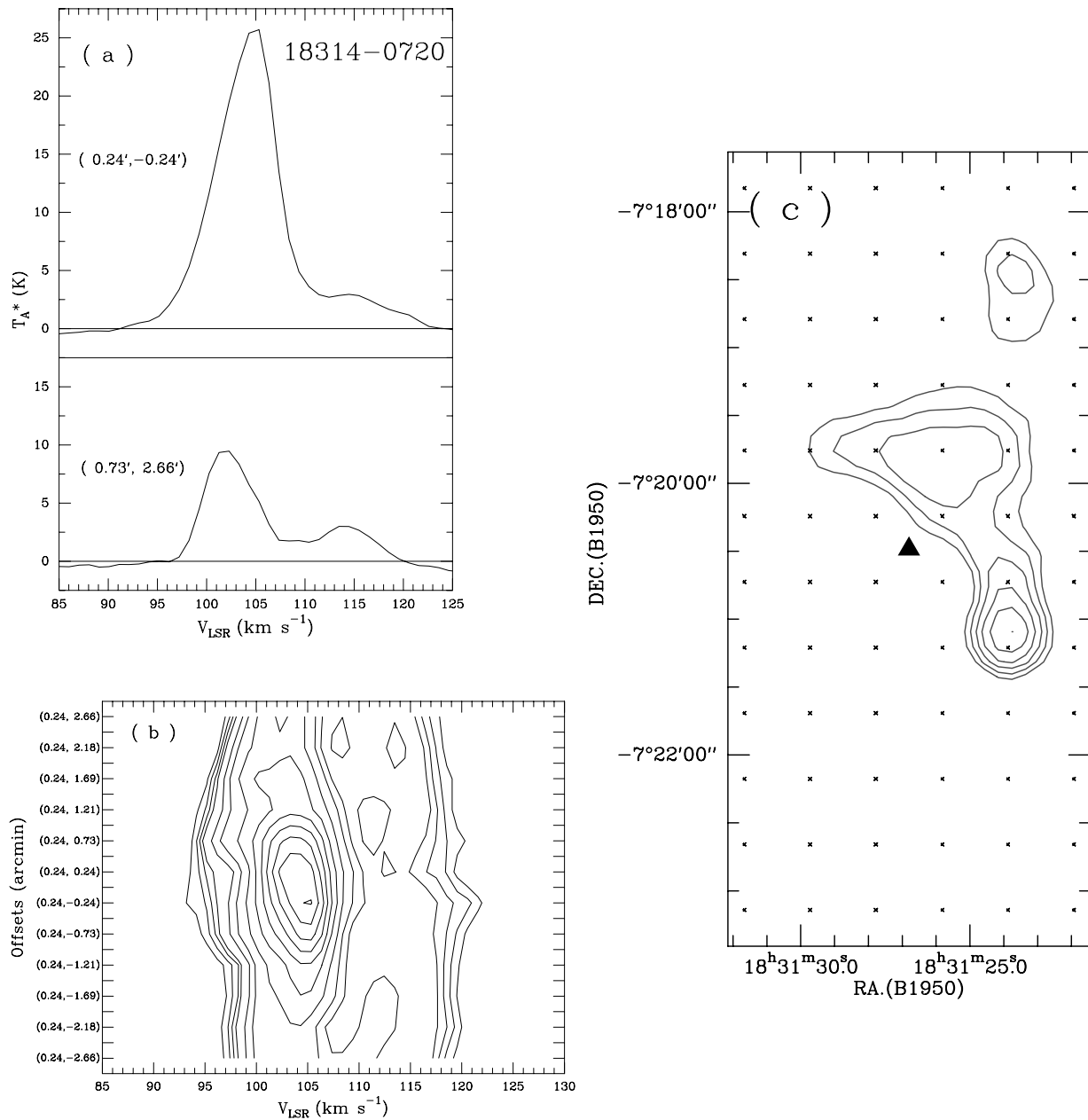


FIG. 7.—Figures for IRAS 18314–0720. (a) Spectra. (b) PV diagram. Levels are at 0.5, 1.0, 1.5, 2.0, 3.5, 5.0, 7.5, 10.5, 13.5, . . . , 37.5 K km s $^{-1}$. (c) Contour map of the blue lobe, integrated over 90.8 to 98.0 km s $^{-1}$. Contour levels are from 12.5 to 19.3 K km s $^{-1}$ by 1.7 K km s $^{-1}$.

red wings in the CO $J = 1-0$ line (Wouterloot & Brand 1989). Yang & Wu (2000) mapped the CO $J = 1-0$ line and identified an outflow associated with a high-mass YSO. Molinari et al. (1998) observed HCO $^+$ and SiO, and an outflow was detected. They also measured emission at 15 μ m and 3.4 mm. The spectra of CO $J = 2-1$ in Figure 6a show that the CO $J = 2-1$ lines also have asymmetric profiles and wings. The total width (-61.7 to -41.8 km s $^{-1}$) is larger than that of CO $J = 1-0$ (-57.9 to -41.3 km s $^{-1}$). Molinari et al. (1998) set $V < -53$ km s $^{-1}$ as the blue wing and $V > -47$ km s $^{-1}$ as the red wing for the SiO spectra. Our high-velocity ranges are defined by the PV diagram along the outflow axis (north-south direction), which is presented in Figure 6b. The PV diagram clearly shows no high-velocity gas less than -46 km s $^{-1}$ at the redshifted side. We take the high-velocity ranges as $V < -53$ km s $^{-1}$ and $V > -46$ km s $^{-1}$ for the blue and red wings, respectively. In both the outflow contours of SiO (Molinari et al. 1998) and CO

$J = 2-1$ of this work, the red lobe is rather diffuse, which is due to the rather small velocity gradient at -47 km s $^{-1}$ and also at -46 km s $^{-1}$. The map of the integrated emission of the blue and red wings (Fig. 6c) shows that the two lobes mostly overlap, which may indicate a nearly pole-on outflow. The spatial extent of the CO $J = 2-1$ outflow is smaller than that of CO $J = 1-0$ (Yang & Wu 2000). The center of the outflow lobes is associated with the peak of the 3.4 mm continuum contours, of which the image is shown in Figure 6c. This image shows that the 3.4 mm compact source, which corresponds to a very young stellar object, probably drives the outflow. The location of IRAS 23385+6053 (see Table 2) is offset about $20''$ from the millimeter emission peak [α (B1950) = $23^{\text{h}}38^{\text{m}}31^{\text{s}}.4$, δ (B1950) = $60^{\circ}53'50''$ (Molinari et al. 1998)]. At the position of α (B1950) = $23^{\text{h}}38^{\text{m}}28^{\text{s}}.5 \pm 1^{\text{s}}.2$, δ (B1950) = $60^{\circ}53'51'' \pm 9''$, a continuum source was detected at 4.85 GHz (Gregory & Condon 1991), which is within the *IRAS* error ellipse ($13'' \times 3''$). Therefore, the

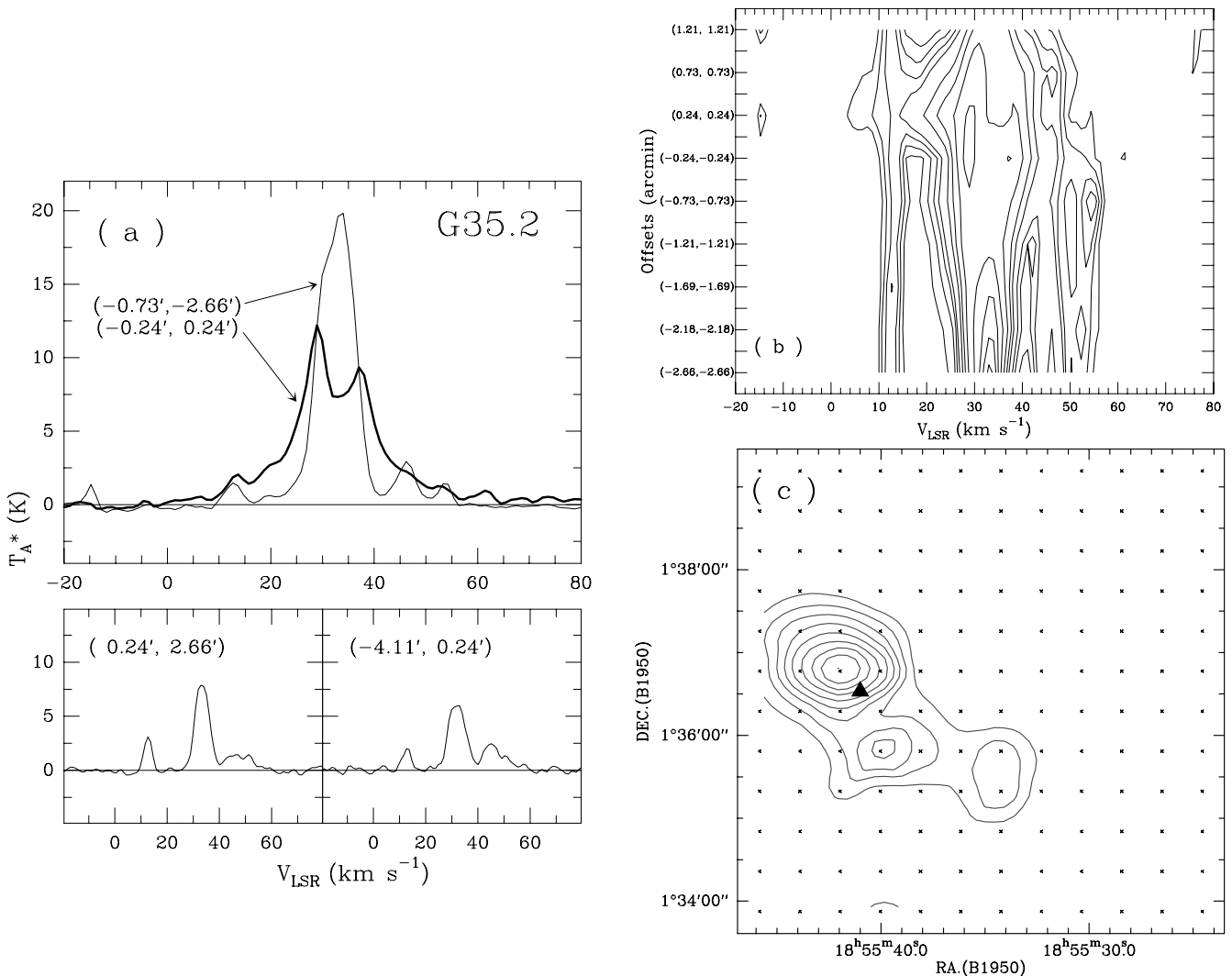


Fig. 8.—Figures for G35.2-0.74. (a) Spectra. (b) PV diagram. Levels are at $0.5, 1.0, 1.5, 2.0, 3.5, 5.0, 7.5, 11.5, 15.5, \dots, 39.5 \text{ K km s}^{-1}$. (c) Contour map of the blue lobe, integrated over 17.7 to 25.0 km s^{-1} . Contours begin at 6.8 K km s^{-1} with increasing steps of 3.4 K km s^{-1} .

Class 0 object mentioned by Molinari et al. (1998) may not be the dominant *IRAS* source but a second, weaker object within the *IRAS* beam. We take the bolometric luminosity of the *IRAS* source as the luminosity of the driving source.

3.2. Sources in which Bipolar Outflows Cannot Be Identified

IRAS 18314-0720.—This is an H II region corresponding to the radio source G24.47+0.49. H₂O maser emission was detected at 102 km s^{-1} by Churchwell et al. (1990). Observations in CO $J = 1-0$ showed a total line width at zero intensity of 34.5 km s^{-1} (Wu et al. 1998a). The CO $J = 2-1$ map in this paper covers a region of $5.6' \times 2.8'$. The line profiles are asymmetric and broad. Two spectra taken from $(\Delta\alpha, \Delta\delta) = (0.24', -0.24')$ and $(-0.73', 2.66')$ are shown in Figure 7a. The spectrum in the top panel seems to show both blue and red wings. However, in the spectrum in the bottom panel, we can see a minor peak at 114 km s^{-1} , about 10 km s^{-1} from the main component. The emission of this red peak remains constant throughout the map and represents a component of extended emission. Meanwhile, the blue wing extends more than 12 km s^{-1} from the line center, indicative of high-velocity wings. Figure 7b shows the PV diagram. We can see again the extended cloud components at the redshifted side. The contours of the blueshifted emission is mainly distributed in the west and the north of the

central source (Fig. 7c). The redshifted emission cannot be identified because of the confusion by the other component.

G35.2-0.74.—It is a strong H₂O maser source (Comoretto et al. 1990 and references therein). Dent et al. (1984) mapped the H II region at 6 cm. The dominant source in the region, *IRAS 18556+0136*, has color indexes higher than the criteria for H II regions and a luminosity of $1.6 \times 10^4 L_{\odot}$ at a distance of 2 kpc. A weaker *IRAS* source, *IRAS 18556+0139*, is located $3'$ north of the reference position. Matthews et al. (1984) observed the region in the HCO⁺ $J = 1-0$ and $J = 3-2$ lines. They reported a bipolar outflow in the northern part of the source around $\alpha(\text{B1950}) = 18^{\text{h}}55^{\text{m}}41^{\text{s}}$, $\delta(\text{B1950}) = 01^{\circ}36'45''$. Dent et al. (1985) mapped the source in CO $J = 1-0$ and CS $J = 2-1$. They obtained a CO bipolar outflow and a CS core. Our CO $J = 2-1$ map was made with an offset position $\alpha(\text{B1950}) = 19^{\text{h}}07^{\text{m}}14.7$, $\delta(\text{B1950}) = 00^{\circ}06'22''$, which is cleaner than the one used by Dent et al. (1985). The size of the map is larger than the HCO⁺ and the CO $J = 1-0$ maps. The CO $J = 2-1$ results show that there are more than two cloud components. Four CO $J = 2-1$ spectra taken from different positions are shown in Figure 8a, of which one is from the central region near *IRAS 18556+0136* and the others are from the edge region. Lines are very broad in the central region around *IRAS 18556+0136*. There is a strong self-absorption at the line center. This agrees

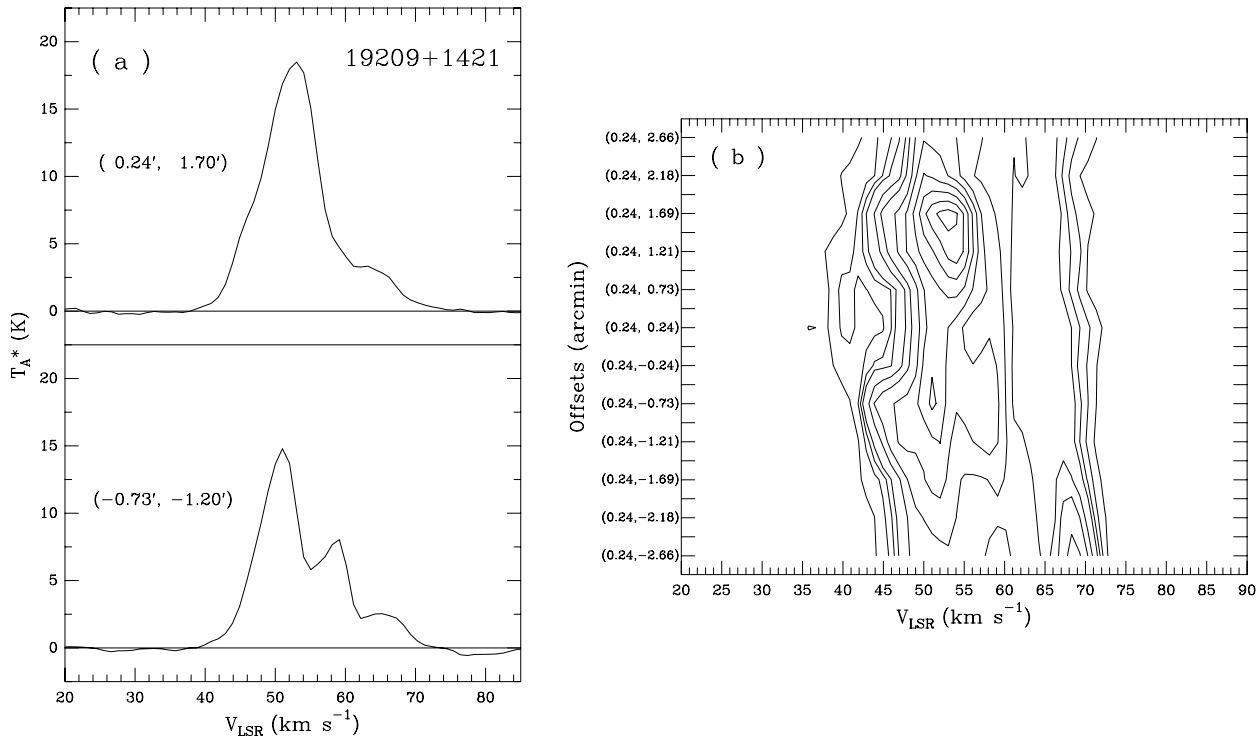


FIG. 9.—Figures for IRAS 19209+1421. (a) Spectra. (b) PV diagram. Contour levels are at 0.5, 1.0, 1.5, 2.0, 3.5, 5.0, 7.5, 9.5, 11.5, ..., 19.5 K km s⁻¹.

well with previous observations. In the entire region, there are perhaps five components at $-14.2, 12.8, 32.7, 44.6$, and 53.2 km s⁻¹, respectively. The PV diagram (Fig. 8b) shows weak velocity components at about 10, 40, and 50 km s⁻¹. Excluding the component at 12.8 km s⁻¹, we made contours for the blueshifted wing of the main component. The range of integration is from 17.7 to 25 km s⁻¹. The map is shown in Figure 8c. The blue lobe is consistent with that of Dent et al. (1985). The red lobe cannot

be determined because of the additional component at 44.5 km s⁻¹. In the CO $J = 1-0$ results of Dent et al., the red wing is adopted as 40–48 km s⁻¹, which includes the 44.5 km s⁻¹ component.

IRAS 19209+1421.—This source is located in the west of W51 at a distance of 6.8 kpc (Genzel & Downes 1977). It is a strong *IRAS* source with a luminosity of $7.7 \times 10^5 L_\odot$. Its *IRAS* color indexes satisfy the criteria of UC H II regions. H₂O maser

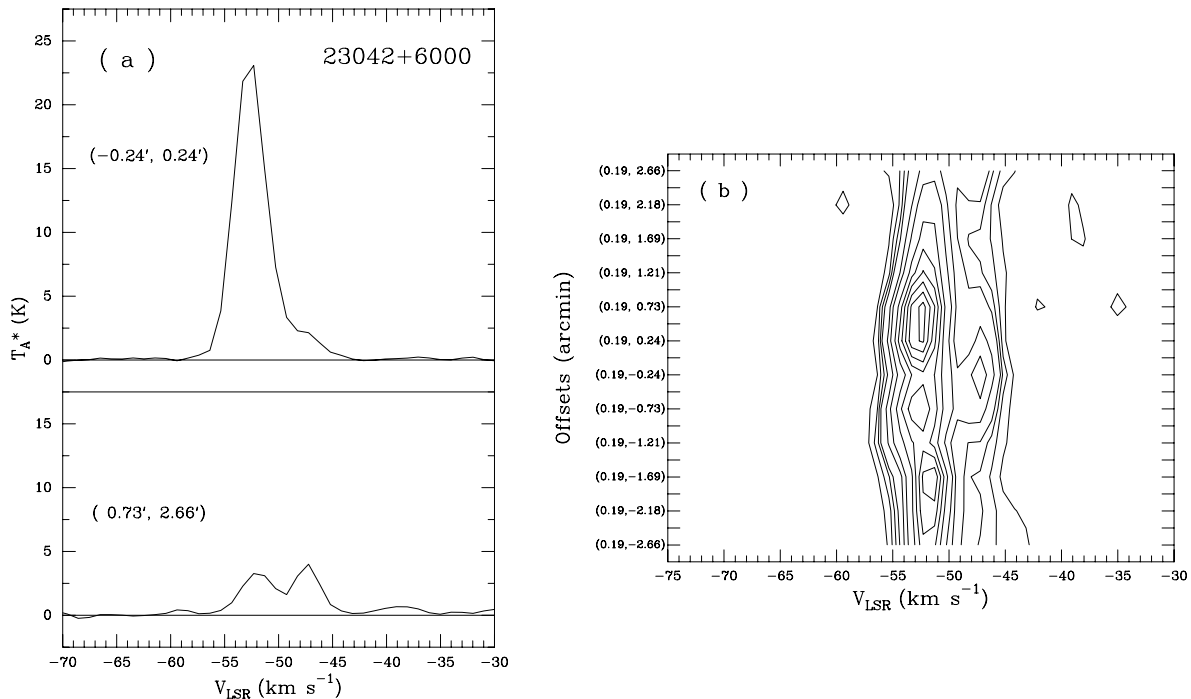


FIG. 10.—Figures for IRAS 23042+6000. (a) Spectra. (b) PV diagram. Contour levels are at 0.5, 1.0, 1.5, 2.0, 3.5, 5.0, 7.5, 9.5, 11.5, ..., 19.5 K km s⁻¹.

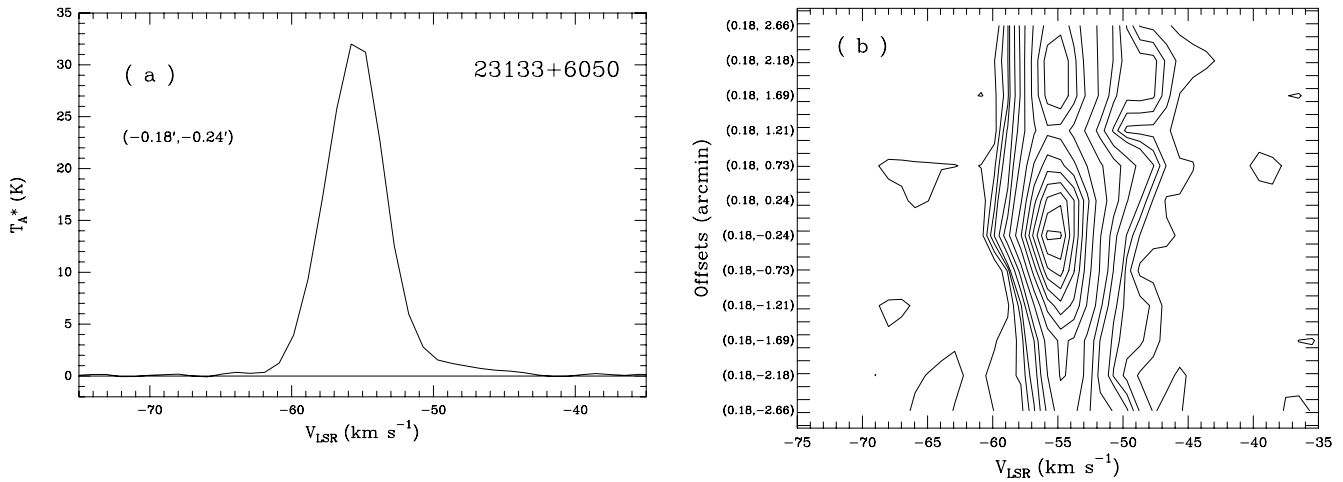


FIG. 11.—Figures for IRAS 23133+6050. (a) Spectrum. (b) PV diagram. Levels are at 0.5, 1.0, 1.5, 2.0, 3.5, 5.0, 7.5, 9.5, 11.5, . . . , 39.5 K km s⁻¹.

emission at about 52.0 km s⁻¹ with multiple components has been detected at $(\Delta\alpha, \Delta\delta) = (17'', 14'')$ southwest of IRAS 19209+1421 (Genzel & Downes 1977; Comoretto et al. 1990). Two CO $J = 2-1$ spectra are shown in Figure 9a. The peak emission is at 53 km s⁻¹. The spectrum in the top panel has blue and “broad” red wings. The one in the bottom panel presents two additional components at about 58 and 66 km s⁻¹. There is likely the high-velocity blue wing, but the red wing is confused by these two velocity components.

IRAS 23042+6000.—This is the only *IRAS* source within the mapped region. The *IRAS* color indexes satisfy the criteria of UC H II regions. Wouterloot & Brand (1989) observed it in the CO $J = 1-0$ line and found two components at -53.3 and -47.9 km s⁻¹. The CO $J = 1-0$ lines observed by Wu et al. (1998b) have a width at zero intensity of about 26 km s⁻¹. Two CO $J = 2-1$ spectra are shown in Figure 10a. The one taken from the central region at $(\Delta\alpha, \Delta\delta) = (-0''.24, 0''.24)$ shows a velocity range from -58.5 to -43.0 km s⁻¹ at zero intensity. The spectrum taken from the northern edge at $(\Delta\alpha, \Delta\delta) = (0''.73, 2''.66)$ shows two components at -52.7 and -47.5 km s⁻¹, respectively. The velocities of the two components agree with those of the CO $J = 1-0$ (-53.3 and -47.89 km s⁻¹). However, the relative intensities are different. (The beam sizes of the telescopes used in the two observations are about the same.) In the central region, the two CO $J = 1-0$ components are 15.6 and 13.9 K, respectively (Wouterloot & Brand 1989), whereas for the CO $J = 2-1$, the T_A^* of the two components are about 23.5 and 2.5 K, respectively. In addition, in the $J = 2-1$ line, the component at -52.7 km s⁻¹ decreases rapidly toward the edge, but the component at -47.5 km s⁻¹ remains constant. This may

suggest that the excitation conditions are different for these two components. These two components can also be seen in the PV diagram (Fig. 10b).

IRAS 23133+6050: This is the only *IRAS* source within the mapped region. The *IRAS* color indexes satisfy the criteria of H II regions. VLA observations show strong emission at 3.6 and 2.0 cm wavelengths (Kurtz et al. 1994). The center of the radio source G111.612+0.374 is at $\alpha(B1950) = 23^h13^m21^s.25$, $\delta(B1950) = 60^{\circ}50'49''.5$, which coincides with the *IRAS* source. The CO $J = 1-0$ line shows a large line width (24.3 km s⁻¹ at zero intensity) and broad wings (Wu et al. 1998b), similar to the CO $J = 2-1$ line in Figure 11a. Figure 11b shows its PV diagram.

4. DISCUSSION

4.1. Comparison between Results of the CO $J = 2-1$ and the CO $J = 1-0$ Lines

The velocity extents of line wings differ between the CO $J = 1-0$ and $J = 2-1$ lines. For OMC 2, the CO $J = 2-1$ velocity ranges from -7.5 km s⁻¹ to around 25 km s⁻¹, whereas it is from 0 to 20 km s⁻¹ for CO $J = 1-0$ (Fischer et al. 1985). In GGD 27 and IRAS 22543+6145, the total widths in the CO $2-1$ line are 48 (from -8 to 40) km s⁻¹ and 61.6 (from -40 to 21.6) km s⁻¹, respectively. These are much larger than the widths in the CO $J = 1-0$ line (6–19 km s⁻¹ and -36 to 14 km s⁻¹, respectively; Yamashita et al. 1989; Rodríguez et al. 1980a). The total CO $J = 2-1$ widths for other bipolar outflows (S146 and IRAS 23385+6053) are also larger than those of CO $J = 1-0$ by 5–10 km s⁻¹ (see Yang & Wu 1998, 2000). The

TABLE 4
PARAMETERS OF OUTFLOWS

Source	Size (pc)	M (M_{\odot})	P (M_{\odot} km s ⁻¹)	E (10^{45} ergs)	t (10^4 yr)	L (L_{\odot})	F ($10^{-3} M_{\odot}$ km s ⁻¹ yr ⁻¹)	\dot{M} ($10^{-5} M_{\odot}$ yr ⁻¹)
OMC 2.....	0.10	3.1	27	2.6	1.1	1.9	2.5	0.5
GGD 27.....	0.25	27	240	25	1.1	19	22	4.4
S146.....	0.66	51	540	43	5.4	6.4	9.9	2.0
IRAS 22506+5944.....	0.38	55	670	69	2.3	24	29	5.8
IRAS 22543+6154.....	0.13	3.1	76	14	0.57	20	13	2.6
IRAS 23385+6053.....	0.52	23	226	17	4.0	3.5	5.6	1.1

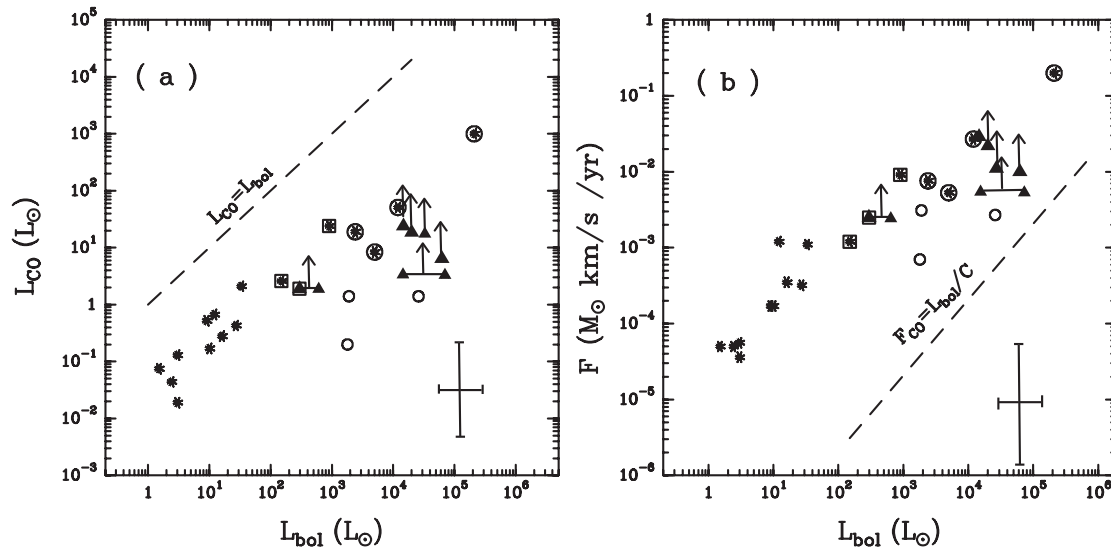


FIG. 12.—Correlations of outflow parameters: (a) mechanical luminosity vs. bolometric luminosity; (b) driving force vs. bolometric luminosity. Sources from Cabrit & Bertout (1992) are plotted as stars, of which those for massive sources (with $L_{bol} > 1000 L_{\odot}$) are put in circles and those for intermediate-mass ones (with L_{bol} between 100 and 1000 L_{\odot}) in squares. Sources from Shepherd & Churchwell (1996b) are plotted as open circles. Sources from this work are plotted as triangles, of which the one for OMC 2 is plotted in a square. The uncertainties in the parameters are shown in the bottom right corner.

spatial extent of the CO 2–1 outflow for OMC 2 agrees in general with the result of the CO $J = 1$ –0 outflow (Fischer et al. 1985) but is narrower in the northwest-southeast direction. For GGD 27, the outflow regions measured with the CO $J = 2$ –1 line are smaller than those of the CO $J = 1$ –0 line with the same integration range. For IRAS 22543+6145, the half-power contour of the CO $J = 2$ –1 outflow is smaller than that of CO $J = 1$ –0, even considering the different spatial resolutions and the different velocity intervals of the cores (Rodríguez et al. 1980a). In S146 and IRAS 23385+6053, the outflow regions are smaller than those measured in the CO $J = 1$ –0 line.

The mass of the CO $J = 2$ –1 outflows may not be compared directly with those of the CO $J = 1$ –0 line for several reasons: the ratio of $[\text{H}_2]/[^{12}\text{CO}]$ used, the excitation temperature adopted, the line intensity measured, the area of the flow region determined, and the velocity range of the wings chosen. For those in which masses can be compared, the masses of the CO $J = 2$ –1 outflows are usually smaller than those of the CO $J = 1$ –0 line.

The broader line wings seen in the CO $J = 2$ –1 line suggest that outflows in massive star-forming regions arise from relatively warm gas. Calculations show that under LTE conditions, the CO $J = 2$ –1 line is expected to be stronger than the CO $J = 1$ –0 line for gas temperatures of more than 20 K. We found that the peak brightness temperature exceeds 20 K in regions observed here. In addition to the benefit of achieving higher angular resolution compared to the CO $J = 1$ –0 line, the CO $J = 2$ –1 line is more sensitive to warm outflows. These warm gases are localized to the massive YSOs in massive star-forming regions.

4.2. Outflow Parameters

We analyzed the relationship between the outflow parameters and the properties of the driving source identified as above. The outflow parameters are listed in Table 4. It appears that the outflows in high-mass star-forming regions carry significantly larger amount of masses and momenta than those of low-mass outflows. Since high-mass stars typically form in a cluster with

members of lower masses, there have been suggestions that high-mass outflows are driven by low-mass YSOs in the cluster. However, the masses and momenta in high-mass outflows are at least an order of magnitude larger than in typical low-mass outflows (Cabrit & Bertout 1992; Myers et al. 1988). The sensitivity and spatial resolution of our observations are not high enough to detect single molecular outflows driven by individual low-mass stars. Assuming a Salpeter initial mass function and a scaling law of outflow mass-loss rate and the luminosity of the star (see Tan & McKee 2002), the molecular outflow from low-mass stars can exceed the mass-loss rate from the massive star alone and dominate the flow in the cluster. Observationally, this has not been confirmed. Since the axes of low-mass outflows are not necessarily aligned in the cluster, they contribute to the blue- and red-shifted gas randomly. Thus, one should expect to observe in many outflows in massive star-forming regions that the blue- and redshifted lobes overlap spatially, if low-mass outflows follow the scaling law. This is not what has been observed: at an spatial resolution of 30'', we resolve the outflows toward S146 and IRAS 22543+6145. At 11'' resolution, Beuther et al. (2002a) shows toward a larger sample that outflow lobes from massive star-forming regions are spatially well separated. In addition, higher angular resolution data from radio interferometers (e.g., Shepherd et al. 1998, 2000; Beuther et al. 2002b, 2003; Su et al. 2004) also show that these outflows are associated with the more massive members in the cluster. Thus, it is most likely that the high-mass YSOs drive the high-mass outflows.

To further analyze the relationship between the outflow parameters and the driving sources, we plotted the correlation in Figure 12. For comparison, we also included sources from Cabrit & Bertout (1992) and Shepherd & Churchwell (1996b). Figures 12a and 12b show the correlation between the CO outflow luminosity L_{CO} and L_{bol} , and the mechanical force and L_{bol} , respectively. The bolometric luminosity of the central source is calculated with the IRAS fluxes. They are close to the results derived from other infrared observations (see Wu et al. 2004). Mechanical luminosity and the force required by the outflow have most of their uncertainty from the mass determination.

However, when the value of τ increases toward the line center, the outflow velocity itself decreases. Thus, the gas with velocity closer to the line center, although its mass is larger, does not contribute to momentum and energy as much as mass. The effect of optical depth on momentum and energy is partially removed by the decreased velocity itself. Here we still take the factor of 5 (see § 3) possibly introduced by the assumption of optically thin emission to account for the uncertainty of the mass. The excitation temperature T_{ex} is usually assumed to equal to T_d and T_k . In general, T_d is equal or greater than T_k , with a difference of less than 10 K (Wu & Evans 1989). It can introduce 30% uncertainty to mass estimates. Besides the uncertainty introduced by mass, the projection effect may bring an uncertainty of a factor of 2 to the momentum and a factor of 3 to the energy (Goldsmith et al. 1984). Consequently, the possible maximum uncertainty is $(5^2 + 0.3^2 + 2^2)^{1/2} \simeq 5.4$ for the CO outflow momentum P and force F and $(5^2 + 0.3^2 + 3^2)^{1/2} \simeq 6.0$ for the CO outflow mechanical luminosity, L_{CO} . The uncertainty is presented in Figure 12 by error bars. More discussion of uncertainties in outflow parameters can be found in Cabrit & Bertout (1990).

One can see that the mechanical force of the outflow is larger than the radiation pressure of the driving source. In addition, the mechanical luminosity of the CO outflow is less than the bolometric luminosity of the stellar source for all the outflows. However, the ratio $L_{\text{bol}}/L_{\text{CO}}$ is about 10 for low- and intermediate-mass stars and about 100 or more for massive stars on average. As for the ratio $F/(L_{\text{bol}}/c)$, where c is the speed of light, the situation is the opposite. These correlations confirm that the momentum and energy of an outflow are related to the properties of the stellar object. This relation was reported by Bally & Lada (1983) when studying a limited sample of molecular outflows.

Recently, controversy has arisen regarding the relation between the mass flow rate and the bolometric luminosity of the central source. Shepherd & Churchwell (1996b) reported a relation between the mass flow rate and the bolometric luminosity that can be better fit by a second-order polynomial. Beuther et al. (2002a) found that the second-order fit is an upper envelope in the high-mass regime. To investigate this relation further, we plot the two parameters in Figure 13 using up-to-date data (Wu et al. 2004). The sample includes 257 sources with available outflow mass, dynamic time, and the bolometric luminosity of the central source. The data are more heterogeneous than the project sources of this paper because they were quoted from different surveys (Wu et al. 2004 and references therein). Besides the effect of optical depths (see § 3), the assumed or derived T_{ex} could introduce an uncertainty of 60%. The difference in the assumed ratio of $[\text{H}_2]/[\text{CO}]$ may bring an uncertainty of a factor of 2 (Ridge & Moore 2001) and can reach a maximum of a factor of 4. The uncertainty in the mass of outflows is a factor of 6.4, based on the above estimates. The possible maximum uncertainty is shown in Figure 13 with error ranges. In Figure 13, the sample is divided into three groups on the basis of the luminosity of the central objects. Asterisks indicate low-mass sources with $L_{\text{bol}} \leq 100 L_{\odot}$, high-mass sources with $L_{\text{bol}} > 1000 L_{\odot}$ are denoted with triangles, and the intermediate-mass sources with L_{bol} between 100 and 1000 L_{\odot} are presented as squares. A second-order fit to the data is shown with the dashed line $\log(M/t) = (-5.38 \pm 0.12) + (0.23 \pm 0.10) \log L_{\text{bol}} + (0.05 \pm 0.002)(\log L_{\text{bol}})^2$. This relation is different from the one fitted by Shepherd & Churchwell (1996b; dotted line). The residual standard error of our second-order fit is $\sigma = 0.81$, 2 times that of Shepherd & Churchwell (1996a). However, we find

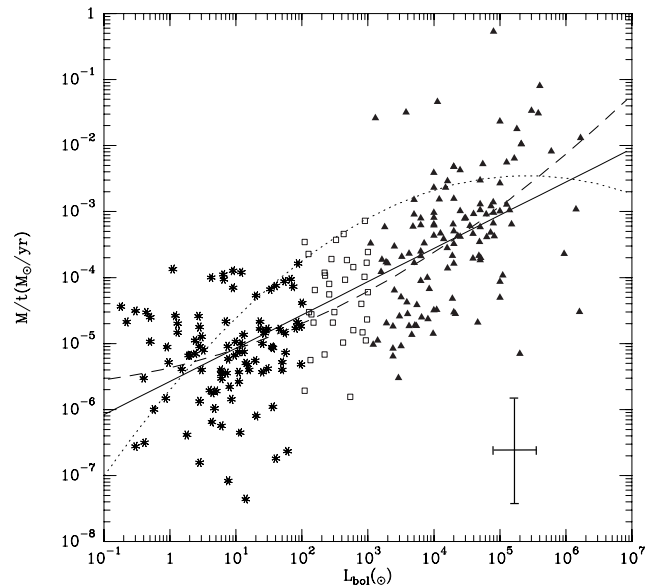


FIG. 13.—Mass-loss rate (M/t) vs. bolometric luminosity. The sample is taken from up-to-date data (Wu et al. 2004 and references therein). Sources with $L_{\text{bol}} \leq 100 L_{\odot}$ are plotted as stars, sources with $L_{\text{bol}} > 1000 L_{\odot}$ are denoted with triangles, and those for intermediate-mass ones (with L_{bol} between 100 and 1000 L_{\odot}) with squares. The uncertainties in the parameters are shown at the lower right corner. The dotted line shows the second-order polynomial fit to the data of Shepherd & Churchwell (1996b) and the references therein. The dashed and solid lines show a second-order fit and a linear fit to the up-to-date data, respectively.

a linear fit is better: $\log(M/t) = (-5.57 \pm 0.096) + (0.50 \pm 0.030) \log L_{\text{bol}}$, with a correlation coefficient of 0.73. Results show that the outflow mass rate increases with increasing bolometric luminosity of the central source, suggesting that the outflow mass rate is related to the luminosity of the central source.

Figure 12 shows that the mechanical forces in CO outflows are more than an order of magnitude higher than the radiation forces from the driving star. This, as in Lada's (1985) analysis, means that if outflows are driven in a momentum-conserving fashion, the radiation pressure from the star cannot drive the outflow. Lada (1985) pointed out that in order for the radiation pressure to be an effective mechanism, photons will need to interact with the medium more than 100 times before escaping the core. After a few scatterings in the medium, photons will be mostly in the IR wavelengths, at which the medium becomes mostly optically thin.

As for thermal pressure in the ionized gas, H II regions at their early stages cannot expand freely, as in the classical picture of H II regions (Spitzer 1978). As shown in Keto (2002, 2003), hypercompact H II regions are trapped in the deep gravitational well of massive stars. The thermal pressure cannot overcome the gravity of the massive star until the ionization front reaches the critical radius at which the escape velocity equals the sound speed of the ionized gas. Thus, the thermal pressure does not drive the outflow at the early evolutionary stage of massive stars. Studies of low-mass outflows have suggested that the infall and accretion drive the outflow. The infalling/accreting materials with excess angular momenta escape the gravitational potential of the star and are directed to the polar axis of the accretion disk (e.g., Shu et al. 2000). It is possible that the high-mass outflows are powered in a similar manner. As in low-mass stars, disks and jetlike outflows have been detected toward high-mass stars (Zhang et al. 1998, 1999; Cesaroni et al. 1997, 1999).

Even though the low- and high-mass young stars bear some similarities during their birth, there are clear differences. We do not have a clear picture as to how high-mass stars are formed. Figure 12 only provides a general trend of continuity between high- and low-mass outflow parameters. Further observational and theoretical studies of molecular outflows hold the promise not only for understanding the driving mechanism of outflows but also the formation of high-mass stars.

5. SUMMARY

We observed the CO $J = 2-1$ line toward 11 massive star formation regions. Results show that all sources display broad emission in line wings. Moreover, the profiles of the lines and the distribution of the high-velocity gas are complex in general. Six sources have bipolar outflows, and outflow parameters were derived. The remaining five sources have one or both line wings confused by additional velocity components. To distinguish outflow emission from contamination of intervening cloud components, mapping in the higher J level CO lines is necessary.

Compared with the outflows detected with the CO $J = 1-0$ line, the CO $J = 2-1$ line wings often extend further in velocity and have smaller spatial extent, indicating that the high-velocity gas measured with the CO $J = 2-1$ line arises from the warm gas closer to the central source.

The masses and momenta of the outflows are higher than those in low-mass outflows. Combining the data of Cabrit & Bertout (1992) and Shepherd & Churchwell (1996b), we discuss

the relation between the outflow parameters and the properties of the driving source. Correlations exist between the luminosity, the mechanical force of the outflow, and the luminosity of the driving sources. For momentum-driven outflows, the radiation pressure from the central source cannot drive the outflow. We reexamine the relation between the mass entrainment (M/t) of the outflows and the bolometric luminosity of the sources with an up-to-date sample. Results show that the mass-loss rate of the outflow increases with increasing source luminosity.

The driving source of these outflows, except IRAS 23385+6053, all correspond to a near-infrared source and are associated with compact radio continuum sources, except IRAS 22506+5944.

We are grateful to the staff at the NRAO 12 m telescope for their assistance in observations. We also wish to acknowledge Jarken Esimbek, Ming Zhao, and Wentao Yu for their help in the VLA data processing and plot preparation. Yuefang Wu thanks the Center for Astrophysics for the assistance and support during her visiting. We thank the anonymous referee for his/her helpful suggestions and comments. We used the data products from 2MASS, a joint project of the University of Massachusetts and the Infrared Processing and Analysis Center/California Institute of Technology, funded by NASA and the NSF. This project was supported by grants 10128306, 10133020 and 10203003 of NSFC and G1999075405 of NKBRSP.

REFERENCES

- Arce, H. G., & Goodman, A. A. 2001, *ApJ*, 554, 132
 —. 2002, *ApJ*, 575, 928
- Bally, J., & Lada, C. J. 1983, *ApJ*, 265, 824
- Beuther, H., Schilke, P., Gueth, F., McCaughrean, M., Andersen, A., Sridharan, T. K., & Menten, K. M. 2002a, *A&A*, 387, 931
- Beuther, H., Schilke, P., Sridharan, T. K., Menten, K. M., & Walmsley, C. M. 2002b, *A&A*, 383, 892
- Beuther, H., Schilke, P., & Stanke, T. 2003, *A&A*, 408, 601
- Blair, G. N., Davis, J. N., & Dickinson, D. F. 1978, *ApJ*, 226, 435
- Blair, G. N., Peters, W. L., & Vanden Bout, P. A. 1975, *ApJ*, 200, L161
- Cabrit, S., & Bertout, C. 1990, *ApJ*, 348, 530
 —. 1992, *A&A*, 261, 274
- Casoli, F., Combes, F., Dupraz, C., Gerin, M., & Boulanger, F. 1986, *A&A*, 169, 281
- Cesaroni, R., Felli, M., Jenness, T., Neri, R., Robberto, M., Testi, L., & Walmsley, C. M. 1999, *A&A*, 345, 949
- Cesaroni, R., Felli, M., Testi, L., Walmsley, C. M., & Olmi, L. 1997, *A&A*, 325, 725
- Chernin, L. M., & Masson, C. R. 1991, *ApJ*, 382, L93
- Choi, M., Evans, N. J., II, & Jaffe, D. T. 1993, *ApJ*, 417, 624
- Churchwell, E. 1999, in *The Origin of Stars and Planetary Systems*, ed. C. J. Lada & N. D. Kylafis (Dordrecht: Kluwer), 515
- Churchwell, E., Walmsley, C. M., & Cesaroni, R. 1990, *A&AS*, 83, 119
- Comoretto, G., et al. 1990, *A&AS*, 84, 179
- Dent, W. R. F., Little, L. T., Kaifu, N., Ohishi, M., & Suzuki, S. 1985, *A&A*, 146, 375
- Dent, W. R. F., Little, L. T., & White, G. J. 1984, *MNRAS*, 210, 173
- Felli, M., & Harten, R. H. 1981, *A&A*, 100, 42
- Felli, M., Harten, R. H., Habing, H. J., & Israel, F. P. 1978, *A&AS*, 32, 423
- Fischer, J., Righini-Cohen, G., & Simon, M. 1980, *ApJ*, 238, L155
- Fischer, J., Sanders, D. B., Simon, M., & Solomon, P. M. 1985, *ApJ*, 293, 508
- Garden, R. P., Hayashi, M., Gatley, I., Hasegawa, T., & Kaifu, N. 1991, *ApJ*, 374, 540
- Genzel, R., & Downes, D. 1977, *A&AS*, 30, 145
- Goldsmith, P. F., Snell, R. L., Hemeon-Heyer, M., & Langer, W. D. 1984, *ApJ*, 286, 599
- Gregory, P. C., & Condon, J. J. 1991, *ApJS*, 75, 1011
- Hartigan, P., & Lada, C. J. 1985, *ApJS*, 59, 383
- Henkel, C., Haschick, A. D., & Guster, R. 1986, *A&A*, 165, 197
- Ho, P. T. P., Moran, J. M., & Rodriguez, L. F. 1982, *ApJ*, 262, 619
- Hughes, V. A., & Wouterloot, J. G. A. 1984, *ApJ*, 276, 204
- Jenness, T., Scott, P. F., & Padman, R. 1995, *MNRAS*, 276, 1024
- Keto, E. 2002, *ApJ*, 568, 754
 —. 2003, *ApJ*, 599, 1196
- Kurtz, S., Churchwell, E., & Wood, D. O. S. 1994, *ApJS*, 91, 659
- Kwan, J., & Scoville, N. 1976, *ApJ*, 210, L39
- Lada, C. J. 1985, *ARA&A*, 23, 267
- Marti, J., Rodriguez, L. F., & Reipurth, B. 1998, *ApJ*, 502, 337
- Matthews, N., Little, L. T., Nyman, L. A., & Macdonald, G. H. 1984, *A&A*, 136, 282
- Molinari, S., Testi, L., Brand, J., Cesaroni, R., & Palla, F. 1998, *ApJ*, 505, L39
- Myers, P. C., Heyer, M., Snell, R. L., & Goldsmith, P. F. 1988, *ApJ*, 324, 907
- Narayanan, G., & Walker, C. K. 1996, *ApJ*, 466, 844
- Rayner, J., McLean, I., McCaughrean, M., & Aspin, C. 1989, *MNRAS*, 241, 469
- Reipurth, B., Rodriguez, L. F., & Chini, R. 1999, *AJ*, 118, 983
- Ridge, N. A., & Moore, T. J. T. 2001, *A&A*, 378, 495
- Rodriguez, L. F., Ho, P. T. P., & Moran, J. M. 1980a, *ApJ*, 240, L149
- Rodriguez, L. F., Moran, J. M., Gottlieb, E. W., & Ho, P. T. P. 1980b, *ApJ*, 235, 845
- Rodriguez, L. F., & Reipurth, B. 1989, *Rev. Mex. AA*, 17, 59
- Shepherd, D. S., & Churchwell, E. 1996a, *ApJ*, 457, 267
 —. 1996b, *ApJ*, 472, 225
- Shepherd, D. S., Watson, A. M., Sargent, A. I., & Churchwell, E. 1998, *ApJ*, 507, 861
- Shepherd, D. S., Yu, K. C., Bally, J., & Testi, L. 2000, *ApJ*, 535, 833
- Shu, F. H., Najita, J. R., Shang, H., & Li, Z.-Y. 2000, in *Protostars and Planets IV*, ed. V. Mannings, A. P. Boss, & S. S. Russell (Tucson: Univ. Arizona Press), 789
- Snell, R. L., Loren, R. B., & Plambeck, R. L. 1980, *ApJ*, 239, L17
- Snell, R. L., Scoville, N. Z., Sanders, D. B., & Erickson, N. R. 1984, *ApJ*, 284, 176
- Spitzer, L., Jr. 1978, *Physical Processes in the Interstellar Medium* (New York: Wiley)
- Su, Y., Zhang, Q., & Lim, J. 2004, *ApJ*, 604, 258
- Tan, J. C., & McKee, C. F. 2002, in *ASP Conf. Ser. 267, The Earliest Stages of Massive Star Birth*, ed. P. A. Crowther (San Francisco: ASP), 267
- Tofani, G., Felli, M., Taylor, G. B., & Hunter, T. R. 1995, *A&AS*, 112, 299
- Torrelles, J. M., Gomez, J. F., Garay, G., Rodriguez, L. F., Curiel, S., Cohen, R. J., & Ho, P. T. P. 1998, *ApJ*, 509, 262
- Wang, J. 1997, Ph.D. thesis, Beijing Astron. Obs.
- Wood, D. O. S., & Churchwell, E. 1989, *ApJ*, 340, 265
- Wouterloot, J. G. A., & Brand, J. 1989, *A&AS*, 80, 149
- Wouterloot, J. G. A., & Walmsley, C. M. 1986, *A&A*, 168, 237
- Wu, Y., & Evans, N. J., II. 1989, *ApJ*, 340, 307

- Wu, Y., Huang, M., & He, J. 1996, *A&AS*, 115, 283
Wu, Y., Wei, Y., Zhao, M., Shi, Y., Yu, W., Qin, S., & Huang, M. 2004, *A&A*, 426, 503
Wu, Y.-F., Li, Y.-X., Lu, J., Sun, J.-J., Lei, C.-M., Wang, L.-M., & Han, F. 1998a, *Acta Astrophys. Sinica*, 18, 415
Wu, Y.-F., Li, Y.-X., & Zheng, L.-F. 1998b, *Chinese Astron. Astrophys.*, 22, 459
Wu, Y.-F., Shi, J.-R., Wang, J.-Z., Jiang, D.-R., & Huang, X.-Y. 1999, *Chinese Astron. Astrophys.*, 23, 454
Yamashita, T., Sato, S., Nagata, T., Suzuki, H., Hough, J. H., McLean, I. S., Garden, R., & Gatley, I. 1987, *A&A*, 177, 258
Yamashita, T., Suzuki, H., Kaifu, N., Tamura, M., Mountain, C. M., & Moore, T. J. T. 1989, *ApJ*, 347, 894
Yang, C.-Y., & Wu, Y.-F. 1998, *Acta Astrophys. Sinica*, 18, 323
_____. 2000, *Acta Astrophys. Sinica*, 20, 141
Yu, K. C., Billawala, Y., & Bally, J. 1999, *AJ*, 118, 2940
Zhang, Q., Hunter, T. R., Brand, J., Sridharan, T. K., Molinari, S., Kramer, M. A., & Cesaroni, R. 2001, *ApJ*, 552, L167
Zhang, Q., Hunter, T. R., & Sridharan, T. K. 1998, *ApJ*, 505, L151
Zhang, Q., Hunter, T. R., Sridharan, T. K., & Cesaroni, R. 1999, *ApJ*, 527, L117
Zuckerman, B., Kuiper, T. B. H., & Kuiper, E. N. R. 1976, *ApJ*, 209, L137